Clementine Observations of the Zodiacal Light
and the Dust Content of the Inner Solar System

Joseph M. Hahn

Lunar and Planetary Institute, 3600 Bay Area Boulevard, Houston, TX 77058
email: hahn@lpi.usra.edu
phone: 281–486–2113
fax: 281–486–2162

Herbert A. Zook[1]

NASA Johnson Space Center, Code SN2, 2101 NASA Road 1, Houston, TX 77058

Bonnie Cooper

Oceaneering Space Systems, 16665 Space Center Boulevard, Houston, TX 77058
email: bcooper@oss.oceaneering.com
phone: 281–228–5332
fax: 281–228–5546

and

Bhaskar Sunkara

Lunar and Planetary Institute, 3600 Bay Area Boulevard, Houston, TX 77058
email: sunnys@cs.uh.edu
phone: 281–480–8304

To appear in *Icarus*

---

[1]passed away on March 14, 2001.

ABSTRACT

Using the Moon to occult the Sun, the Clementine spacecraft used its navigation cameras to map the inner zodiacal light at optical wavelengths over elongations of $3 \lesssim \epsilon \lesssim 30°$ from the Sun. This surface brightness map is then used to infer the spatial distribution of interplanetary dust over heliocentric distances of about 10 solar radii to the orbit of Venus. The averaged ecliptic surface brightness of the zodiacal light falls off as $Z(\epsilon) \propto \epsilon^{-2.45\pm0.05}$ which suggests that the dust cross–sectional density nominally falls off as $\sigma(r) \propto r^{-1.45\pm0.05}$. The interplanetary dust also has an albedo of $a \simeq 0.1$ that is uncertain by a factor of ~ 2. Asymmetries of $\sim 10\%$ are seen in directions east–west and north–south of the Sun, and these may be due the giant planets' secular gravitational perturbations.

We apply a simple model that attributes the zodiacal light as due to three dust populations having distinct inclination distributions, namely, dust from asteroids and Jupiter–family comets (JFCs) having characteristic inclinations of $i \sim 7°$, dust from Halley–type comets having $i \sim 33°$, and an isotropic cloud of dust from Oort Cloud comets. The best–fitting scenario indicates that asteroids + JFCs are the source of about 45% of the optical dust cross–section seen in the ecliptic at 1 AU, but that at least 89% of the dust cross–section enclosed by a 1 AU radius sphere is of a cometary origin. Each population's radial density variations can also deviate somewhat from the nominal $\sigma(r) \propto r^{-1.45}$. When these results are extrapolated out to the asteroid belt, we find an upper limit on the mass of the light–reflecting asteroidal dust that is equivalent to a 12 km asteroid, and a similar extrapolation of the isotropic dust cloud out to Oort Cloud distances yields a mass equivalent to a 30 km comet, although the latter mass is uncertain by orders of magnitude.

1. Introduction

Interplanetary dust is of considerable interest since these grains represent samples of small bodies that formed in remote niches throughout the solar system. Dust grains are liberated when the rocky asteroids collide and when icy comets sublimate during a close approach to the Sun, and this dust is transported throughout the solar system by solar radiation forces. If it is granted that the information carried by this dust is indeed decipherable, then samples of this dust tell us about the conditions in various parts of the solar nebula from which asteroids, comets, and planets subsequently formed. In particular, asteroidal dust tells us of nebula conditions at the boundary between the terrestrial and the giant–planet zones in the solar nebula. And since the long–period comets from the Oort Cloud formed amongst the giant planets, the mineralogy of their dust is indicative of conditions over a vast swath of the solar nebula between $\sim$ 5–30 AU. Information about the outer reaches of the solar nebula is also carried by dust generated by the shorter–period Jupiter–family comets that likely formed in the Kuiper Belt beyond $\sim$ 30 AU.

This dust is also of dynamical interest since the spatial density of these 'trace particles' allows one to simultaneously assess the relative strengths of Poynting–Robertson drag (which drives dust sunwards), the planets' gravitational perturbations (which disturbs dust orbits and sometime confines dust at resonances), and mutual collisions (which fragments and destroys dust). However a deeper understanding of this dust first requires knowledge of the abundance and spatial distribution of asteroidal and cometary dust grains, both of which are the subject of this investigation.

Whipple (1955) performed one of the earliest assessments of the various sources of interplanetary dust. This analysis is essentially a mass–budget that compares the rates at which comets and asteroids produce dust to the rates at which collisions and Poynting–Robertson drag destroy dust. From the very limited data on comets, asteroids, and interplanetary dust that were available at the time, it was concluded that at least 90% of interplanetary dust is of cometary origin (Whipple 1955, 1967). This view prevailed for the next three decades until the Infrared Astronomical Satellite (IRAS) discovered the asteroidal dust bands (Neugebauer *et al.* 1984; Dermott *et al.* 1984). These dust bands are clearly produced by asteroid families, so these observations demonstrate that asteroids are also significant contributors to the interplanetary dust complex, with models indicating that $\sim$ 30–40% of the outer zodiacal light is due to asteroidal dust (Dermott *et al.* 1994; Liou *et al.* 1995). Asteroidal and cometary dust have also been collected in the Earth's stratosphere by U2 aircraft (Brownlee *et al.* 1993). Atmospheric entry velocities can be inferred from these grains, and about 80% of the dust in this sample have low entry velocities consistent with asteroidal orbits. However this finding should be regarded as an upper limit on the true abundance of asteroidal dust in the ecliptic since (*i.*) dust released from low–inclination Jupiter–family comets (JFCs) can also have low entry velocities (see Section 4.2.2), and (*ii.*) the Earth's gravitational focusing naturally selects for low–velocity dust from asteroids (and JFCs as well) over dust from the higher–inclination Halley–type and Oort Cloud comets.

In order to assess the abundances and spatial distributions of asteroidal and cometary dust in

the inner solar system, the following analyzes images of the zodiacal light that were acquired by the Clementine spacecraft while in lunar orbit. Clementine orbited the Moon for about two months in early 1994, ostensibly to study the lunar surface. But a secondary objective of this mission was to image the inner zodiacal light using Clementine's wide-angle navigation cameras. While the Sun was in eclipse behind the Moon, the Clementine star tracker cameras acquired hundreds of images of the zodiacal light over elongations that span the orbit of Venus down to about 10 solar radii. As this is the first scientific application of a star tracker camera, the instrument and its optics are described in detail in Section 2 and Appendix A. Section 3 and Appendix B describe the observations and data reductions, also in some detail due to several artifacts present in the data. However the reader uninterested in these particulars can skip directly to Section 4 where the interplanetary dust model is described and applied. Results are then summarized in Section 5.

2. The Star Tracker Camera

The zodiacal light images studied here were acquired by the Clementine spacecraft's two star tracker cameras. A star tracker is a simple, light–weight, low–power camera designed to acquire wide–angle CCD images of star fields. The spacecraft's two star tracker cameras are designated A and B, and nearly all of the data examined here were acquired by star tracker B. The principle purpose of the star tracker is to aid spacecraft navigation; by comparing the observed star fields to an onboard star atlas, the spacecraft can continuously monitor its orientation. It should be noted that a high–quality photometric imaging capability was *not* a design criterion for this camera. Nonetheless, our close inspection of the data shows that this camera can be used to obtain high–fidelity images once a number of instrumental artifacts are removed from the data. These data reductions are described in detail in Section 3.

A simplified schematic of the star tracker optics is shown in Fig. 1, and a more detailed description of the instrumentation may be found in Lewis *et al.* (1991) and Kordas *et al.* (1995). The camera's principle components are a spherical lens, a fiber optic, and a CCD detector. The focal point of this lens is at its center. As Fig. 1 shows, incident light entering the lens from the left forms an image at the opposite side of the lens, and the fiber optic pipes this light to the CCD. Appendix A shows how to map the CCD's (x, y) coordinates for every pixel into equatorial and ecliptic coordinates.

The CCD detector is a Thomson TH7883 array of 384×576 pixels. The camera's angular field of view is $29.3° \times 44.6°$ and the plate–scale at the optical axis is 0.0756 degrees/pixel. This camera's point spread function has a full width at half maximum of about 2 pixels $\simeq 0.15°$. No filter was used in this camera. The detector has a peak quantum efficiency of about 45% at a wavelength of $\lambda \simeq 8000$ Å (Lewis *et al.* 1991). Figure 2 gives the camera's relative instrumental response and shows that the camera is sensitive to wavelengths of $5000 \lesssim \lambda \lesssim 9000$ Å. Figure 2 also shows the equivalent square bandpass (e.g., one having the same area under the curve as the observed instrumental response) that has a spectral width of $\Delta\lambda = 3490$ Å and a mean wavelength

$\bar{\lambda}$=7370 Å.

It should be noted that this camera also has two serious handicaps. The first is that the 8–bit CCD has a dynamic range of only 256. However the star tracker images were acquired at exposures that differ by up to a factor of 14, so the total dynamical range of the zodiacal map produced here is $14 \times 256 \simeq 3600$. Another problem is the absence of a shutter in the camera which results in the CCD being continuously exposed as the array is read out along the detector's columns. This tends to redistribute the flux from all sources along the CCD columns. However as Section 3 shows, this effect is reversible, and 'destreaked' data may be recovered from the raw data itself.

3.   Observations and Data Reductions

The Clementine spacecraft was in an elliptical polar orbit about the Moon from February 22 through May 4 of 1994, after which it left the Moon for an encounter with the near–Earth asteroid Geographos and was subsequently lost due to a software failure. But during the final six weeks in orbit about the Moon, the star tracker cameras repeatedly imaged the inner zodiacal light while the Moon occulted the Sun. Numerous images were acquired during an orbit about the Moon, either just prior to sunrise or just after sunset. Each batch of images are identified by an orbit number that is simply the number of lunar orbits that Clementine had achieved to date. Because these observations were acquired during a six week interval, the longitude of the camera's line–of–sight to the Sun changed considerably due to the heliocentric motion of the Earth–Moon system. Table I lists orbit numbers, observation dates, each observation's heliocentric ecliptic longitude, and total exposure times for the subset of the data that are examined here. The camera's lines of sight through the ecliptic during different orbits are also shown in Fig. 3.

All of the raw Clementine data examined here are archived at the National Space Science Data Center and may be obtained at the URL http://nssdc.gsfc.nasa.gov/planetary/lunar/clementine1.html, and the flatfield used to process the star tracker images is available from the authors.

The star tracker camera usually acquired a sequence of about 40 or so images during each orbit of the spacecraft. The exposure times for every image acquired during a sequence usually cycled between 0.05, 0.1, 0.2, 0.4, and 0.7 seconds. By cycling the exposure times in this manner, the camera's dynamic range was increased by a factor of 14 and difficulties due to image–saturation in the brighter parts of the zodiacal light were mitigated. A typical raw image is shown in Fig. 4A, which is a 0.4 sec exposure acquired during orbit 193. Although the Sun is well behind the lunar limb, the Moon is partly illuminated by sunlight reflected by an Earth that is outside of the field of view. The bright object left of the Moon is a saturated Venus. In fact, Venus is so bright that the signal accumulating in the pixel at Venus has bled into the nearest 10 or so pixels.

Note also the bright streak at Venus in Fig. 4A as well as a broader but dimmer streak running through the core of the zodiacal light. These streaks are a consequence of reading the CCD array in

a shutterless camera. The camera electronics reads the CCD array by shifting the contents of every pixel down along the CCD's columns that, in Fig. 4, run left–to–right. As a row of "logical" pixels shifts off the bottom of the array, their values are recorded, zeroed, and then that row shifts back into the CCD's top row. However the CCD is always exposed during this process, so reading out the CCD array causes every logical pixel to receive additional signal from all parts of the sky that subtend that pixel's CCD column. This results in an image that appears to have streaks running along the columns (see Fig. 4A). Nonetheless, the time to transfer the contents of one pixel to the next, 94.4 μsec (Kordas *et al.* 1995), is a fixed quantity, so the intensity of each column's streak can be inferred and removed from the raw data itself using the destreaking algorithm given in Zook *et al.* (1997). However this algorithm fails whenever a CCD column contains one or more saturated pixels. In this case, the pixels along the entire column are flagged and are subsequently ignored for the remainder of the analysis. Pixels polluted by Venus also disturb the destreaking algorithm, so they are first replaced with a local average of the zodiacal light prior to destreaking and are subsequently discarded (see Fig. 4B).

In principle the dark current should be subtracted before destreaking an image. However the lack of a shutter makes it impossible to directly measure the dark current from these streaked images. Nonetheless, images acquired during orbit 66 show a very dark lunar surface that is shadowed from both the Sun and the Earth, so the flux observed in lunar surface provides a first estimate of the dark current. An aperture is placed on the dark portion of the Moon and an initial estimate of the dark current f is obtained for every image in the sequence. This current is subtracted from each image which is then destreaked. The residual flux δf in that aperture is then examined, and automated software then revises the estimated dark current f appropriately and this cycle repeats until δf has relaxed to zero. A similar algorithm is also used to subtract the dark current from all of the other images acquired during different orbits. However these images generally show a lunar surface that is either slightly or wholly illuminated by earthshine, so the flux measured in the lunar aperture represents the dark current plus a nonzero offset δf. In this case, the above algorithm iteratively subtracts the dark current f and destreaks each image until a *predetermined* residual flux $\delta f > 0$ is achieved. The value for δf appropriate for each image–sequence is determined later by comparing images that overlap the orbit 66 field; see below.

The construction of the star tracker flatfield is described in Appendix B. Each image is flatfielded and pixels that subtend the Moon are flagged and discarded. Next, small shifts to the images are applied as needed so that the stars seen in an image–sequence appear stationary. A single averaged "master" image is then formed from the image–sequence using only the good pixels that were not previously flagged as bad. Figure 4B shows the master image for orbit 193; the data–gaps correspond to the Moon as well as pixels polluted by Venus.

Two additional faint artifacts become evident upon close inspection of this longer–exposure image. The first is that every eighth column (which runs left–right in Figure 4B) is slightly darker than its neighbors. It is only evident at the outer edges of the images where the zodiacal light is quite faint, and its effect is barely discernible in Fig. 4B. This is probably due to a slight inhomogeneity

in the dark–current across the CCD. However this faint striping is of little consequence since its magnitude is comparable to the noise in the data. Another faint dark stripe can also be seen in the rows that subtend Venus; its magnitude is roughly twice the pixel–to–pixel noise in the image. The cause of this stripe is unknown, and it is only seen in images containing a deeply saturated Venus.

Figure 4C shows a textbook quality image of the zodiacal light which has the Moon and Venus pasted back in.

The camera's plate–scale and its pointing are determined from the handful of bright field stars that are identified in each of the master images; see Appendix A for details. Using each star's observed (x, y) coordinates, their known equatorial coordinates (α, δ), and Eqns. (A1) and (A6), a plate–scale of $p = 0.0756$ degrees/pixel is obtained. The lens coordinates (θ, ϕ) for each star are then computed (see Fig. 1 and Eqns. A1), and Eqns. (A3) are solved for (α_o, δ_o), which are the equatorial coordinates for the pixel at the camera's optical axis, and τ, which is the angle between the CCD's y axis and equatorial north. With these quantities known, equations (A1) and (A3) can now be used to compute equatorial coordinates for every pixel in each master image, and Eqs. (A5) are used to rotate these coordinates into geocentric ecliptic longitude and latitude (Λ, Θ), as well as the longitude of each pixel relative to the Sun, $\Lambda - \Lambda_\odot$.

With the pointing for every master image known, it is now possible to determine the unknown offsets δf for the remaining master images that have not yet had their dark current properly subtracted. By examining those fields that overlap the orbit 66 field, it is straightforward to estimate the small offsets δf that yield a mutually consistent surface brightness in the overlapping regions. This process is then repeated for the remaining adjacent fields until all offsets for all images have been determined. With these new offsets in hand, the entire data–reduction cycle (dark current subtraction, destreaking, flatfielding, and offset determination) is repeated until no further changes in the offsets are required.

The final step is to merge all of the master images into a single wide–angle mosaic of the inner zodiacal light. This results in the $60° \times 60°$ mosaic shown in Fig. 5. This image is formed by mapping the intensity of every good pixel in all of the master images into the corresponding 2×2 box of pixels in the mosaic, which smooths the mosaic over an angular scale of $2p = 0.15°$. Also recall that these images were acquired over a six week interval, so some stars are seen more than once as they drift to the right with time due to the heliocentric motion of the spacecraft. Consequently, several planets are also seen at multiple longitudes: Saturn is barely discernible at about $11°$ west of the Sun, Mars appears at $16°$ and $18°$ west, Saturn again at $19°$, and Mercury at $27°$ west. If the saturated Venus were not already clipped from these images, it would inhabit the data–gap at $20°$ east of the Sun,

The observed intensity of β Hydri is used to calibrate these data. This G2IV star is the only bright object in these images having a solar–type spectrum. This star has $B - V$ and $U - B$ colors that are solar to within 0.05 magnitudes, has an apparent V magnitude of $m_\star = 2.80$, and has

an instrumental intensity of $I_\star = 770 \pm 60$ counts/sec. Note that this intensity is obtained from images that are flatfielded using the "point–source" flatfield that is described in Appendix B. One common brightness unit in zodiacal light observations is the mean solar brightness $B_\odot = I_\odot/\Omega_\odot$, which is the intensity of the Sun $I_\odot$ divided by the solid angle of the Sun $\Omega_\odot = 0.223$ deg^2. Since $I_\star = I_\odot 10^{-0.4(m_\star - m_\odot)}$ for a solar–type star, it follows that

$$1 \text{ count/sec/pixel} = 10^{-0.4(m_\star - m_\odot)} \frac{\Omega_\odot}{\Omega_p} \left(\frac{I_\star}{\text{counts/sec}} \right)^{-1} B_\odot \qquad (1)$$

where $m_\odot = -26.78$ is the apparent visible magnitude of the Sun and $\Omega_p = p^2 = 5.72 \times 10^{-3}$ deg^2 is the solid angle of a pixel at the optical axis. Another common unit is $S10_\odot = 4.33 \times 10^{-16} B_\odot$, which is the intensity of a tenth magnitude solar type star distributed over a square degree. Thus $1 \text{ count/sec/pixel} = (7.5 \pm 0.6) \times 10^{-14} B_\odot = (170 \pm 10) S10_\odot$. The seemingly large uncertainty of 8% in this calibration constant is due to (a) β Hydri's short exposure time of only 0.6 sec, and (b) noise in the flatfield—see Appendix B.

However the relative uncertainties in the mosaic image, Fig. 5, vary across of the field due to the different exposure times of the various master images (see Table I). The fields west of Sun, which were acquired during orbits 66 and 110, had very short exposure times, so the western side of the mosaic is considerably noisier than the eastern side. Uncertainties in the dark current subtraction are ~ 3 counts/sec $\sim 2 \times 10^{-13} B_\odot \sim 500 S10_\odot$. However this uncertainty is significant only at the outer edges of Fig. 5 where it can be as much as 50% of the signal there. We also note that nearly all of the images acquired during orbit 164 had a bright Earth in its field of view, so these images have considerable amounts of scattered light in them. This is the field just north of the Sun in Fig. 5, and this polluted zone lies at elongations of $\Phi \gtrsim 10°$ north and north–northwest of the Sun. This is the only field acquired by star tracker A for which the flatfield is unavailable. We have elected to process this field using the flatfield from star tracker B, and it is included in the mosaic Fig. 5 solely for the purpose of filling an otherwise large datagap. The light–polluted portion of this field is not used in the subsequent analysis.

Faint, diffuse background light from the galaxy also contaminates Fig. 5. However this was minimized by observing at an epoch when the sunward lines of sight were at the highest possible galactic latitudes of $30° \lesssim \beta_g \lesssim 90°$ (see Fig. 3). The surface brightness of the galaxy was measured by Pioneer 10 while at heliocentric distances $r > 2.8$ AU where the zodiacal contribution is negligible; at latitudes $\beta_g > 30°$ the galactic surface brightness is $Z_g < 90 \ S10_\odot$ (Leinert *et al.* 1998) at the southern edge of Fig. 5, and it decreases to the north. However this flux is substantially smaller than the uncertainty in the dark current subtraction and is neglected here.

The integrated intensity of the light seen in Fig. 5 is $I = 4.8 \times 10^{-8} I_\odot$ which corresponds to a visual magnitude $m_V = -8.5$. This makes the zodiacal light the second brightest object in night sky, the first being the full Moon having $m_V = -12.7$ and the third being Venus with $m_V = -4.6$ at its brightest.

4. A Simple Model of the Interplanetary Dust Complex

In order to extract the gross properties of the observed dust seen in Fig. 5, a simple model that is quite common in the literature shall be fitted to these data [*c.f.*, Leinert (1975)]. The model assumes that the dust density varies radially as a power–law with heliocentric distance and that the cloud is axially symmetric. This model also assumes that the center of the cloud is at the Sun and that its midplane is in the ecliptic. Although none of these assumptions are actually correct in detail, they are sufficiently good for our purposes. In this case the spatial density of dust cross–section σ can be written as a function of the heliocentric distance r and heliocentric ecliptic latitude β:

$$\sigma(r,\beta) = \sigma_1 \left(\frac{r}{r_1}\right)^{-\nu} h(\beta) \tag{2}$$

where $r_1 = 1$ AU is a reference distance, $\sigma_1 = \sigma(r_1, 0)$ is the dust cross–section density in the ecliptic at $r = r_1$, and $h(\beta)$ describes how the dust density falls off with ecliptic latitude.

The surface brightness of the sunlight reflected by this dust distribution is proportional to $\sigma(r,\beta)$ multiplied by a light–scattering function and integrated along an observer's line–of–sight. The flux density of sunlight that is reflected by dust in a small volume element dV is $dF = \sigma(r,\beta)\Phi(\varphi)(L_\odot/4\pi r^2)dV/\Delta^2$ (Lester *et al.* 1979) where $dV = \Omega\Delta^2 d\Delta$ and Ω is the solid angle of the volume element as seen by an observer a distance Δ away; see Fig. 6 for the definition of all the geometric quantities used here. The scattering phase function $\Phi(\varphi)$ is related to the phase law $\psi(\varphi)$ via $\Phi(\varphi) = (a/\pi \text{ sr})\psi(\varphi)$ where a is the dust geometric albedo and φ is the scattering angle. Note that this formulation is valid only in the geometric optics limit, which is indeed the case since the bulk of the dust cross–section is contributed by grains having sizes ~ 10–100 μm (Grün *et al.* 1985).

The surface brightness of the zodiacal light is thus $Z = \int dF/\Omega$ integrated over $0 \leq \Delta < \infty$. Noting that $r/r_1 = \sin\epsilon/\sin\varphi$ where ϵ is the elongation of the line of sight having a geocentric ecliptic latitude and longitude (θ, ϕ) relative to the Sun, then $\cos\epsilon = \cos\phi\cos\theta$, $\Delta/r_1 = \sin(\varphi - \epsilon)/\sin\varphi$, $d\Delta/r_1 = \sin\epsilon\, d\varphi/\sin^2\varphi$, and so the surface brightness can be recast as an integral over the scattering angle φ (Aller *et al.* 1967; Giese and Dziembowski 1969):

$$Z(\theta,\phi) = \frac{a\sigma_1 r_1}{\sin^{\nu+1}\epsilon} \left(\frac{\Omega_\odot}{\pi \text{ sr}}\right) B_\odot \int_\epsilon^\pi \psi(\varphi)h(\beta(\varphi))\sin^\nu(\varphi)d\varphi \tag{3}$$

where $\Omega_\odot = 0.223$ deg$^2 = 6.80 \times 10^{-5}$ sr is the solid angle of the Sun and $B_\odot = L_\odot/4\pi r_1^2\Omega_\odot$ is the mean surface brightness of the Sun where $L_\odot$ is the solar luminosity. Note also that the β in Eq. 3 depends on the scattering angle φ through $\sin\beta = \sin(\varphi - \epsilon)\sin\theta/\sin\epsilon$.

4.1. Radial variations

For a line of sight in the ecliptic, $h(0) = 1$ and Eq. (3) becomes a simple integral over the phase law $\psi(\varphi)$. Two very different empirical phase laws are shown in Figure 7. The upper curve was constructed by Lamy and Perrin (1986), and it exhibits a very strong forward scattering peak (*i.e.*, ψ diverges as $\varphi \to 0$) as might occur due to the diffraction of sunlight by dust larger than a wavelength. The lower phase law is from Hong (1985); although this law does not show any forward scattering, it does exhibit a mild backward scattering peak at $\varphi \simeq 180°$ as is required of any phase law in order to reproduce the gegenshein. Despite the very different forms for $\psi(\varphi)$, both phase laws are very able at reproducing a varied suite of other zodiacal light measurements that were acquired over a wide range of elongation angles ϵ (Hong 1985; Lamy and Perrin 1986). Consequently, our results are remarkably insensitive to the choice of the phase law. Regardless of whether one adopts Hong's backscattering phase function or Lamy and Perrin's forward scattering phase law, a numerical integration of the Eq. (3) yields a surface brightness $Z(\epsilon)$ that, over our observation interval $2 \lesssim \epsilon \lesssim 30°$, is largely indistinct aside from a numerical factor of $\simeq 1.6$. This insensitivity to the details of $\psi(\varphi)$ is due to the fact that the dominant contribution to the surface brightness integral is by dust in the vicinity of $\varphi \simeq 90°$, *i.e.*, dust nearer the Sun along the line–of–sight.

This particular behavior also means that the integral in Eq. (3) is quite insensitive to the lower integration limit for the range of elongations $\epsilon \lesssim 30°$ that are considered here. In this case the line of sight integral evaluates to $\simeq 0.83$ when the Hong phase law is used and $\simeq 1.3$ when the Lamy and Perrin law is used. Eq. (3) then simplifies to

$$Z(\epsilon) \simeq (2.3 \pm 0.5) \times 10^{-5} \frac{a\sigma_1 r_1}{\sin^{\nu+1} \epsilon} B_\odot \tag{4}$$

where the error in the coefficient indicates the uncertainty in the phase law. We also note that about 90% of the light seen in the ecliptic at elongations $\epsilon \leq 30°$ is contributed by dust orbiting interior to 0.6 AU.

The radial power law ν is now readily obtained from profiles of the zodiacal light's ecliptic surface brightness. East–west and north–south profiles are shown in Fig. 8, and a power–law fit to the averaged east–west profile yields

$$Z(\epsilon) = \frac{(1.7 \pm 0.2) \times 10^{-13}}{\sin^{2.45\pm0.05} \epsilon} B_\odot \tag{5}$$

so a comparison with Eq. (4) shows that $\nu = 1.45 \pm 0.05$ and $a\sigma_1 r_1 = (7.4 \pm 1.8) \times 10^{-9}$. The uncertainty in the former quantity includes the statistical variations of the data seen in Fig. 8 while the latter quantity also includes the 8% uncertainty in the calibration and the uncertainty due to the possible choices for the phase law. Note that the power law ν reported here is slightly steeper than that inferred from the data obtained by the Helios spacecraft (Leinert *et al.* 1981) and the Cosmic Background Explorer (COBE) spacecraft (Kelsall *et al.* 1998), with the disagreements at the 2σ level.

Figure 8 also reveals an asymmetry in the surface brightness of the zodiacal light north/south of the ecliptic, as well as an asymmetry east/west of the Sun. Ratios of the north/south and east/west surface brightness profiles are plotted in Fig. 9 which shows that the northern hemisphere gets steadily brighter with elongation relative to the southern hemisphere, as does the eastern ansa relative to the western ansa. Asymmetries such as these have been attributed to the giant planets' secular gravitational perturbations which can organize the longitudes of the dust grains' perihelia and nodes (Wyatt *et al.* 1999). The north–south asymmetry seen here is likely the same asymmetry previously observed by the Helios 1 and 2 which detected a $i = 3°$ tilt between the midplane of the inner zodiacal light and the ecliptic (Leinert *et al.* 1980). The node of this symmetry plane has a longitude of $\Omega = 87°$ which, as Fig. 3 shows, is largely perpendicular to the Clementine lines–of–sight, and this particular viewing geometry will make one hemisphere slightly brighter than the other. Gravitational perturbations by giant planets can also displace the zodiacal cloud's center of light radially away from the Sun, which results in a phenomenon known as pericenter glow (Wyatt *et al.* 1999); such perturbations may be responsible for the east–west asymmetry seen in Figs. 8–9.

A comment on the Lamy and Perrin volume scattering function is also in order. Lamy and Perrin (1986) adopt a volume scattering function Ψ (which is proportional to the product $a\sigma_1\psi$ used here) that varies with heliocentric distance as $r^{-\nu_c}$ where ν_c is chosen so that the dust cross sectional density $\sigma(r)$ falls off as $r^{-\nu_1}$ where $\nu_1 = 1$. Although Lamy and Perrin (1986) provide excellent arguments to motivate their approach, their assumption will not be adopted here, but only because we wish to compare our findings to other studies of the zodiacal cloud that similarly do not apply this assumption. However our findings reported below are easily recalibrated if the Lamy and Perrin volume scattering function is preferred. If it is assumed that Ψ does indeed vary as $r^{-\nu_c}$ then this implies that the dust albedo also varies as the power law $a(r) \equiv a_1(r/r_1)^{-\nu_c}$ where a_1 is the dust albedo at $r = 1$ AU. Accounting for this alternate interpretation thus requires the substitutions $a \rightarrow a_1$ and $\nu \rightarrow \nu_1 + \nu_c$ in Eqs. (3–4), but this has no substantive effect on their form. The only significant changes to our findings would be (*i.*) that the albedo quoted in Section 4.3 should be interpreted as the albedo a_1 for dust at 1 AU and that (*ii.*) the integrated dust surface densities and masses given in Eqs. (10–13) need to be reevaluated for the alternate dust density power–law ν_1. But as long as ν_c (which might be as large as 0.45) is smaller than unity then these revisions will change our finding by factors that are also of of order unity.

4.2.   Vertical variations

Estimates of the dust grains' vertical distribution is obtained by first developing a simple yet plausible model for the dust inclination distribution $g(i)$. The dust latitude distribution $h(\beta)$ is then calculated from this inclination distribution, and a surface brightness map of the model dust cloud is generated using the line–of–sight integral Eq. (3). Then by comparing isophotes of the model cloud to the observations (Fig. 5), the suite of dust models that are consistent with the observations are readily obtained below.

4.2.1. inclination distributions

Section 4.2.2 will describe the various inclination distributions $g_j(i)$ for distinct dust–sources *i.e.*, the asteroids, comets, and interstellar sources that are indicated by the j subscript. The relationship between population j's latitude distribution $h_j(\beta)$ and its inclination distribution $g_j(i)$ is

$$h_j(\beta) = \int_\beta^{\pi/2} \frac{g_j(i)di}{\sqrt{\sin^2 i - \sin^2 \beta}} \tag{6}$$

(Divari 1968; Divine 1993; Brown 2001). Although Eq. (6) is formally derived for bodies in circular orbits, it nonetheless provides reliable results even for bodies in very eccentric orbits [c.f. Brown (2001)]. Note that an isotropic cloud has an inclination distribution $g_j(i) = (2/\pi) \sin i$ which results in a latitude distribution $h_j(\beta) = 1$. Accordingly, the total distribution will be written as a sum over several possible components, one being an isotropic source with an *iso* subscript and the N other sources having a gaussian distribution of inclinations:

$$g_j(i) = \frac{2}{\pi} \sin i \times \begin{cases} 1 & j = \text{iso} \\ c_j e^{-(i/\sigma_j)^2/2} & \text{otherwise} \end{cases} \tag{7}$$

where σ_j is the standard deviation of each component's inclination distribution and c_j is a normalization constant such that $h_j(0)$ is unity. If each population's cross–sectional density is assumed to vary as a distinct power–law $\propto r^{-\nu_j}$, then the zodiacal light's total surface brightness becomes [see Eqn. (3)]

$$Z(\theta, \phi) = \sum_j f_j Z_j(\theta, \phi) = a\sigma_1 r_1 \left(\frac{\Omega_\odot}{\pi \text{ sr}}\right) B_\odot \sum_j \frac{f_j}{\sin^{\nu_j+1} \epsilon} \int_\epsilon^\pi \psi(\varphi) h_j(\beta(\varphi)) \sin^{\nu_j}(\varphi) d\varphi. \tag{8}$$

where the coefficients f_j indicate each population's relative contribution to the cross–sectional density in the ecliptic at $r_1 = 1$ AU. Of course each population may also have a distinct albedo a_j, in which case the f_j in Eq. (8) should be replaced by $(a_j/a)f_j$ where a is the 'effective' albedo that would be obtained if only a single dust population was responsible for all of the zodiacal light. However the individual albedos of asteroidal and cometary dust are not known with any certainty so we will simply set $a_j/a = 1$.

4.2.2. source populations

The inclination distribution for the meteoritic dust complex is related to the inclinations of the sources of that dust, namely, colliding asteroids, active dust–producing comets, and interstellar dust sources. The upper portion of Fig. 10 shows the inclination distribution of near–Earth, main–belt, and Trojan asteroids. The smooth curve in this figure also shows that the observed inclination distribution can be qualitatively represented by the form $g(i) \propto \sin i e^{-(i/\sigma)^2/2}$ with $\sigma = 6.2°$. Note, however, that this curve seriously undercounts asteroids with inclinations $i > 20°$ that are about 6% of the total asteroid population.

The inclination distributions for comets having perihelia $q < 2.5$ AU that are presumably active producers of dust are also shown in Fig. 10 where they are divided into three dynamical classes: the Jupiter–family comets (JFCs), the Halley–type comets (HTCs), and the Oort Cloud comets (OCCs). The JFCs have the lowest inclinations since they likely originated in the (relatively) low–inclination Kuiper Belt (Levison and Duncan 1997). Conversely, the wide–ranging OCCs have the highest inclinations since their orbital planes have been randomized by the galactic tide and passing stars (Duncan *et al.* 1987). However the HTCs have intermediate inclinations as they likely originate in a somewhat flatted inner Oort Cloud (Levison *et al.* 2001). The smooth curves in Fig. 10 also show representative inclination distributions with $\sigma = 8°$ for the JFCs, $\sigma = 33°$ for the HTCs, and $g(i) \propto \sin i$ for the isotropic OCCs. Interstellar dust should also be distributed isotropically in the inner solar system and thus have a similar inclination distribution. Note, however, that these cometary σ's should be regarded as rough estimates since the apparent orbital distributions suffer from selection effects that tend to favor the discovery of comets in low–perihelia, low–inclination orbits. In fact, the underabundance of high–inclination OCCs in Figure 10 suggests that selection effects may be especially severe for these single–apparition comets.

Evidently, there are three classes of dust sources having distinct inclination distributions: a lower inclination population composed of asteroids and JFCs having a $\sigma_{low} \simeq 7°$, a higher inclination population composed of HTCs having a $\sigma_{high} \simeq 33°$, and an isotropic population of dust from OCCs and interstellar sources. With these σ's in hand, the normalization coefficients c_j appearing in Eq. (7) are obtained by numerically integrating Eq. (6) and requiring $h_j(\beta = 0)$ equal unity, which yields $c_{low} = 10.27$ and $c_{high} = 2.190$.

The remainder of this study shall assume that the dust observed in Fig. 5 have the same inclination distributions as their source populations. However this need not necessarily be true since dust grains will slowly spiral sunward due to Poynting–Robertson (PR) drag. As a consequence of this radial mobilization, dust grains can traverse secular resonances with the planets where they can experience additional inclination excitation. The degree of this excitation is size dependent since a larger particle will drift at a slower rate across a resonance and thus experience greater inclination excitation. Dynamical models indicate that grains with radii $R \gtrsim 100$ μm will suffer significant inclination–pumping, *i.e.* $\Delta i \gtrsim 10°$, whereas grains smaller than $R \lesssim 30$ μm suffer only modest pumping, *i.e.* $\Delta i \lesssim 3°$ (Jackson and Zook 1992; Dermott *et al.* 2001; Grogan *et al.* 2001). However the cross–sectional area of interplanetary dust is dominated by grains having radii 10 μm $\lesssim R \lesssim 100$ μm which peaks at $R \sim 30\mu$m (Grün *et al.* 1985), so this additional source of inclination–excitation is at most a marginally important effect that is not modeled here. But even when a dust grain is far from a secular resonance, the planets secular perturbation will still excite forced inclinations that are of order a few degrees. These latter perturbations, which are also not treated by our model, introduces a warp in the zodiacal cloud whose inclination varies with the dust semimajor axis.

4.3. The abundance of asteroidal and cometary dust

With the inclination distributions characterized, Eq. 7 can be inserted into Eq. 6 and the latitude distributions $h_j(\beta)$ can be evaluated numerically for each population. This in turn allows us to compute maps of each population's surface brightness $Z_j(\theta, \phi)$ on a geocentric latitude-longitude grid using Eq. 8, and isophotes for example populations are shown in Fig. 11. A synthetic surface brightness map of the zodiacal light is formed by selecting the power–laws ν_j for each population, computing the $Z_j(\theta, \phi)$ maps, and then coadding the maps with proportions f_{low}, f_{hi} ,and f_{iso}. Although the synthetic map has seven parameters, $i.e$, three f_j, three ν_j, and $a\sigma_1 r_1$, the available parameter space is quite limited since $0 \leq f_j \leq 1$. Also recall the single power–law evident in the ecliptic surface brightness profile, Fig. 8. The absence of a broken power–law in the ecliptic profiles suggests either (a) all populations have a similar $\nu_j \simeq 1.45$ radial variation, or (b) there is a single population having $\nu_j \simeq 1.45$ that contributes most of the observed light. Note that the asteroidal dust likely varies as r^{-1} which is expected for dust that spirals into the field of view via PR drag[2]. However the cometary components should vary faster than r^{-1} since these dust grains can are produced *in situ* at rates that also vary with distance r. Consequently we expect the three populations to have $1 \lesssim \nu_j \lesssim 2$ or so.

We have scanned the ν_j parameter space between $\nu_j = 1.0$ to $\nu_j = 2.5$ in increments of about $\Delta\nu_j = 0.5$. It is straightforward to scan the remaining f_j parameter space for a given ν_j triplet, and in general there is only a single set of f_j parameters that agrees with the observations in a least–squares sense. Best agreement with the data is achieved when the ν_j and f_j take the parameters listed in Table II with the error bars indicating the range of possible fits that are marginally acceptable. Contours for this model are shown in Fig. 12 which compares quite favorably to the observed isophotes. However a model having all the $\nu_j = 1.45$ and $f_{low} = 0.34 \pm 0.06$, $f_{high} = 0.51 \pm 0.11$, and $f_{iso} = 0.15 \pm 0.06$ yields isophotes that are very similar to Fig. 12 with agreement that is almost as good. This indicates that this model is particularly sensitive to the bright, high–inclination dust population that is distributed over a wide range of latitudes, but that the power–law variations in the low–latitude as well dimmer isotropic populations are less well constrained. In general, we find acceptable solutions only when $1.0 \lesssim \nu_{low} \lesssim 1.45$, $\nu_{high} \simeq 1.45$, and $1.45 \lesssim \nu_{iso} \lesssim 2.0$ having approximate abundances of $f_{low} \sim 0.4$, $f_{high} \sim 0.5$, and $f_{iso} \sim 0.1$.

Recall that there is still a population of high inclination asteroids having $i_{ast} \sim 22°$ that have not yet been considered (see Fig. 10); these asteroids represent about 6% of the total asteroid population. Might these asteroids be a significant source of the high latitude dust seen in Fig. 5? If so, then their fractional contribution to the ecliptic surface brightness would be of order $f_{ast} \sim 6\% f_{low}\sigma_{low}/i_{ast} \sim 0.01$ when smeared out over an annulus that is $i_{ast}/\sigma_{low} \sim 3$ times thicker than that inhabited by the lower–i asteroids. Consequently, these high–i asteroids are not likely to

---

[2]This assertion is true when the dominant light–reflecting grains have an orbital lifetime due to PR drag that is shorter than their collision lifetimes, which is the case for grains having radii smaller than about ~ 100 μm (Grün *et al.* 1985).

be a significant source of high–latitude dust since their ecliptic contribution is only $\sim 2\%$ that of the high–inclination population's contribution f_{high}.

The inferred dust latitude distribution $h(\beta)$ is also shown in Fig. 13 as well as the weighted contributions $f_j h_j(\beta)$ by the low, high, and isotropic dust populations. This figure shows that at ecliptic latitudes $\beta > 15°$, more than 90% of the cross–section is contributed by dust that are in comet–like orbits (e.g., HTCs and OCCs). The spatial distribution of the dust cross section is also shown in Figure 14. Although these contours are rather similar to that inferred by Kelsall *et al.* (1998) from the COBE observations, they do differ in detail due to the different assumptions built into each model. Specifically, the Kelsall *et al.* model employs an empirical function (namely, a modification of the familiar fan model) to describe the dust latitude distribution $h(\beta)$ of their 'smooth cloud' (which is the principle component of that model), whereas we allow for three distinct distributions $h_j(\beta)$ that are instead based upon known comet and asteroid inclination distributions. Although both modeling efforts adopt very different treatments of the dust latitude distributions $h(\beta)$, and these models were also applied to data acquired at rather different wavelengths (optical versus near and far infrared), the inferred dust density distributions reported here and by Kelsall *et al.* (1998) are quite similar. The density distribution given in Fig. 14 is also reminiscent of the familiar fan model that assumes $\sigma(r, \beta) = \sigma_1(r/r_1)^{-\nu} e^{-k|\sin\beta|}$. However a parameterization of this form provides at best only a qualitatively correct estimation of the density map of Fig. 14 when $k \simeq 1.5$; it still fails to reproduce this Figure in detail, especially at high latitudes beyond $\beta \gtrsim 45°$ and at distances beyond $r \gtrsim 2$ AU.

The inferred inclination distributions for all of the dust populations are also shown in Fig. 15. We also note also that these distributions are rather similar to that reported by Divine (1993) who inferred dust size and orbital distributions from a wide suite of dust observations (e.g., microcraters on lunar samples, spacecraft dust–impact experiments, as well as other zodiacal light observations). However Divine did not comment on the implications of this inclination distribution, which we regard as one of the more interesting findings of this study.

Since $\sigma_j(r, \beta) = f_j \sigma_1 (r/r_1)^{-\nu_j} h_j(\beta)$ is the density of population j's dust cross–section, its total dust cross–section contained within a sphere of radius r is obtained from the volume integral

$$\Sigma_j(r) \;=\; \int \sigma(r, \beta) dV \tag{9a}$$

$$=\; \frac{f_j \gamma_j}{3 - \nu_j} \left(\frac{r}{r_1} \right)^{3 - \nu_j} 4\pi \sigma_1 r_1^3 \tag{9b}$$

where the latitude integration is $\gamma_j \equiv \int_0^{\pi/2} h_j(\beta) \cos \beta d\beta$, which numerically integrates to $\gamma_{low} = 0.143$, $\gamma_{high} = 0.619$, and $\gamma_{iso} = 1.00$. Adopting the best–fitting ν_j and f_j parameters given in Table II, each population's total dust cross–section interior to $r_1 = 1$ AU is $\Sigma_j(r_1) = \{0.032, 0.200, 0.050\} \times 4\pi \sigma_1 r_1^3$, respectively, for the low, high, and isotropic populations. Although the low–inclination dust from asteroids and JFCs contributes $f_{low} = 45\%$ of the dust cross–sectional density in the ecliptic, at least 89% of the dust interior to a $r_1 = 1$ AU sphere is contributed by sources in comet–like

orbits (e.g., HTCs and OCCs plus an unknown fraction from JFCs).

Using data from spacecraft dust collection experiments as well as studies of lunar microcraters, Grün et $al.$ (1985) estimate the spatial density of the ecliptic dust cross section at 1 AU to be $\sigma_1 \sim 4.6 \times 10^{-21}$ cm^2/cm^3. Since Table II reports $a\sigma_1 r_1 = (7.4 \pm 1.8) \times 10^{-9}$, this implies that the dust have an effective albedo of $a \simeq 0.1$. Note, however, that these estimates for σ_1 and thus a are probably uncertain by a factor of ~ 2 since these dust collection experiments largely measure dust fluxes versus particle energy, and that their conversion to a dust cross–section requires assumptions about the dust velocities and their bulk densities.

Summing Eq. (9b) over all populations yields the total dust cross–section contained within a sphere of radius r:

$$\Sigma(r) = 2.0 \times 10^{10} \left[0.032 \left(\frac{r}{r_1} \right)^2 + 0.200 \left(\frac{r}{r_1} \right)^{1.55} + 0.050 \left(\frac{r}{r_1} \right) \right] \text{ km}^2 \tag{10}$$

where each term gives the contribution by the low i, high i, and isotropic populations, respectively. Note that this expression only applies interior to the dust–producing portion of the asteroid belt, $i.e.$ interior to $r \simeq 3.3$ AU (Hanner et $al.$ 1974). If we consider a sphere of radius $r_2 = 2$ AU enclosing the orbits of the terrestrial planets, then $\Sigma(r_2) = 1.6 \times 10^{10}$ km^2, which is about 50 times the total cross–section of the terrestrial planets. This estimate illustrates one of the main difficulties challenging efforts to detect extra–solar planets via direct imaging or interferometry at optical wavelengths: if terrestrial extra–solar planets are also embedded in solar system–like dust, then one will need to resolve planetary systems to fairly small spatial scales in order to discriminate the starlight reflected by planets from that reflected by dust.

The Pioneer 10 spacecraft detected asteroidal dust out to a heliocentric distance of $r_3 \simeq 3.3$ AU (Hanner et $al.$ 1974), so Eq. (9b) indicates that the low–inclination dust component has a total surface area $\Sigma_{low}(r_3) = 6.8 \times 10^9$ km^2. Note that observations of the IRAS dust bands serve as a comforting reality check on our findings since the total surface area associated with the three most prominent asteroidal dust bands is $\Sigma_{band} = 4.7 \times 10^9$ km^2 (Grogan et $al.$ 2001); the remaining dust must then be due to other minor asteroid families, non–family asteroids, and JFC comets. Also, if the light–reflecting dust seen in Fig. 5 can be attributed to grains having a characteristic radius R_c, then the total number of grains interior to distance r is $N_j(r) \sim \Sigma_j(r)/\pi R_c^2$ and their enclosed mass $M_j(r) \sim 4\rho R_c \Sigma_j(r)/3$ is

$$M_j(r) \sim \frac{16\pi R_c \sigma_1 \rho r_1^3 f_j \gamma_j}{3(3 - \nu_j)} \left(\frac{r}{r_1} \right)^{3 - \nu_j} \tag{11}$$

where ρ is the grains' bulk density. In this case the total mass of the light–reflecting component of asteroidal dust is at most of order

$$M_{low}(r_3) \sim 2.3 \times 10^{18} \left(\frac{\rho}{2.5 \text{ gm/cm}^3} \right) \left(\frac{R_c}{100 \ \mu\text{m}} \right) \text{ gm.} \tag{12}$$

The interplanetary dust mass distribution peaks at $R_c \sim 100$ μm (Grün *et al.* 1985), so the above dust mass–limit is equivalent to an asteroid that is about 12 km across. Of course this limit is valid only if our model, which is based on observations of dust orbiting at $r \lesssim 0.6$ AU, can be reliably extrapolated out to the asteroid belt. Nonetheless, the similarity between our dust model and that inferred from the COBE observations, which are sensitive to dust in the $1 \lesssim r \lesssim 3$ AU interval (Kelsall *et al.* 1998), indicate that our extrapolation is indeed valid. We also note that the mass limit obtained here about 3.5 times the mass of the asteroidal dust bands detected by COBE (Reach *et al.* 1997), but keep in mind that our limit is also contaminated by dust from JFCs.

The isotropic cloud of dust is also quite interesting, and the following discussion assesses the relative dust contribution from Oort Cloud comets versus interstellar sources. The dust seen in Fig. 5 having a typical elongation of $\epsilon \sim 15°$ orbit at a heliocentric distance of $r \sim r_1 \sin \epsilon \sim 0.3$ AU, and this dust has a cross–sectional density of $\sigma_{iso}(0.3 \text{ AU}) = f_{iso}\sigma_1(0.3 \text{ AU}/r_1)^{-\nu_{iso}} \sim 3 \times 10^{-21}$ cm^2/cm^3 in the ecliptic. The interstellar fraction is inferred from the flux of interstellar dust measured by impact detectors onboard the Galileo and Ulysses spacecraft. These detectors measured an interstellar dust flux of $f_\star = 1.5 \times 10^{-8}$ grains/cm^2/sec [after correcting a typo in Grün *et al.* (1997)]. These interstellar grains have a mean mass of $m_\star \sim 3 \times 10^{-13}$ gm, so their characteristic radius is $R_\star \sim 0.3$ μm. It will be assumed here that the interstellar dust flux is roughly constant throughout the solar system since radiation pressure roughly balances solar gravity for grains of this size. Since interstellar matter approaches the solar system with a velocity–at–infinity of $v_\infty = 25$ km/sec (Frisch 2000), the number density of interstellar dust is $n_\star \sim f_\star/v_\infty \sim 6 \times 10^{-15}$ cm^{-3} and their cross–sectional density is $\sigma_\star \sim \pi R_\star^2 n_\star \sim 2 \times 10^{-23}$ cm^2/cm^3. This is only about 1% of the observed cross–sectional density σ_{iso}, which indicates that the isotropic portion of the dust seen in Fig. 5 comes predominantly from Oort Cloud comets.

Oort Cloud comets have semimajor axes $a \sim 10^4$ AU, and those comets passing sufficiently close to the Sun will sublimate gas and dust that gets injected into orbits similar to their parent comets. If we naively extrapolate these wide–ranging dust grains out to Oort Cloud distances using the inferred $\nu_{iso} = 2$ radial power–law, the total Oort Cloud dust mass is

$$M_{iso} \sim 1 \times 10^{19} \left(\frac{\rho}{1 \text{ gm/cm}^3} \right) \left(\frac{R_c}{1 \text{ }\mu\text{m}} \right) \left(\frac{a}{10^4 \text{ AU}} \right) \text{ gm,} \qquad (13)$$

which has a equivalent to a ~ 30 km comet. However this mass is easily uncertain by orders of magnitude due to uncertainties in the size and bulk density of the dust as well as the radius of the Oort Cloud. Ultimately these distant dust grains will be stripped from the solar system as they are swept up by the interstellar gas and dust that flows through the solar system. Thus it is conceivable that the Sun also has a vast but tenuous tail of Oort Cloud dust. If so, this dust tail would be oriented in the downstream direction of the local interstellar flow which has a heliocentric ecliptic longitude, latitude of $(74.7°, -4.6°)$ (Frisch 2000) or an equatorial right ascension, declination of $(73.9°, +18.0°)$.

5. Summary and Conclusions

Using the Moon to occult the Sun, the Clementine spacecraft used its navigation cameras to map the inner zodiacal light at optical wavelengths over elongations of $3 \lesssim \epsilon \lesssim 30°$ from the Sun. Since the zodiacal light is sunlight that is reflected by interplanetary dust, this map provides a measure of the dust grains' radial and vertical variations spanning heliocentric distances of $0.05 \lesssim r \lesssim 0.6$ AU, $i.e.$, from about 10 solar radii to just interior to Venus' orbit. The integrated zodiacal light seen over the $60° \times 60°$ field of view has a visible magnitude $m_V = -8.5$, indicating that the meteoritic complex is one of the brightest members of the planetary system, second only to the full Moon.

The averaged ecliptic surface brightness of the zodiacal light falls off as $Z(\epsilon) \propto \epsilon^{-2.45\pm0.05}$ which suggests that the dust cross–sectional density nominally varies as $\sigma(r) \propto r^{-1.45\pm0.05}$ (but see below). This surface brightness also indicates that the dust obey $a\sigma_1 r_1 = (7.4 \pm 1.8) \times 10^{-9}$. Assuming that the dust have an ecliptic cross–sectional density of $\sigma_1 = 4.6 \times 10^{-21}$ cm^2/cm^3 at $r_1 = 1$ AU (Grün et $al.$ 1985), this implies that the dust have an effective albedo of $a = 0.1$ that is perhaps uncertain by a factor of 2. Asymmetries of $\sim 10\%$ in the zodiacal light's surface brightness are evident at elongations $\epsilon \sim 15°$ in directions east–west as well as north–south of the Sun, and these asymmetries may be due to the giant planets' secular gravitational perturbations. However simple digital filtering of the data ($i.e.$, unsharp masking) does not reveal any other subtle features such as dust bands associated with asteroid families or dust trails associated with individual comets.

In order to assess the relative contributions to the interplanetary dust complex by asteroids and comets, we have modeled the zodiacal cloud as being due to three dust populations having distinct inclination distributions. One dust population is assumed to have low inclinations that are distributed as a gaussian with a standard deviation $\sigma_{low} \simeq 7°$ that is characteristic of both asteroids as well as Jupiter–Family comets (JFCs). A higher–inclination population corresponding to the Halley–type comets (HTCs) is assumed to have a $\sigma_{high} \simeq 33°$, and the third population is an isotropic cloud of dust from Oort Cloud comets. This simple model is applied to the observations and very good agreement is achieved for the parameters listed in Table II (see Fig. 12). It should be noted that the best–fitting model has a radial power–law $\nu_{low} = 1.0$ for the asteroidal + JFC population, which is consistent with dust delivery via Poynting–Robertson (PR) drag yet shallower than the nominal $\nu = 1.45$ power–law quoted above. Also, the dust from HTC appears to follow a $\nu_{high} = 1.45$ power–law while the Oort Cloud dust varies as $\nu_{iso} = 2.0$. Interstellar dust also contributes to this isotropic cloud, but only at the $\sim 1\%$ level. Yet despite this mixture of power–laws, the resulting surface brightness profile still varies close to the observed $Z(\epsilon) \propto \epsilon^{-2.45}$. Note, however, that acceptable agreement with the data is also achieved when all populations have $\nu_j = 1.45$; see Section 4.3 for the allowed range of model parameters.

The best–fitting model indicates that about $f_{low} = 45\%$ of the dust cross–section in the ecliptic at $r_1 = 1$ AU comes from asteroids and JFCs. But when a 1 AU–radius sphere is considered, at least 89% of the integrated dust cross section comes from sources in comet–like orbits. However

it should be noted that these findings are inferred from a 'static' model of stationary dust grains. This rather simple approach is applicable provided dust grains (and in particular, asteroidal dust) do not experience substantial–inclination pumping as they evolve sunwards due to PR drag and cross orbital resonances with the planets. Although this appears to be the case for grains smaller than $\sim 100~\mu$m that are the dominant source of reflected sunlight, inclination pumping is certainly of greater importance for the larger dust grains that can drift across resonances at slower rates. In this instance, 'dynamic' models that include radiation and gravitational forces are preferred as they can faithfully follow a dust grain's orbital evolution from source to sink, and these more sophisticated models have been used to extract dust properties from the infrared observations of the outer zodiacal light acquired by IRAS (cf. Dermott *et al.* (2001); Grogan *et al.* (2001)). Of course these dynamic dust models are also applicable to the optical observations of the inner zodiacal light examined here, and we suspect that any effort to simultaneously fit a dynamic dust model to the full suite optical and infrared IRAS, COBE, and Clementine observations should yield an even more tightly constrained picture of the interplanetary dust complex spanning a very wide range of heliocentric distances $0.05 \lesssim r \lesssim 3.3$ AU. And in order to facilitate any such effort, the Clementine map of the inner zodiacal light is available from the authors by request.

The inferred cross–section of dust orbiting interior to 2 AU is about 50 times that of the terrestrial planets. This suggests that any effort to directly detect terrestrial extrasolar planets at optical wavelengths is faced with the daunting task of distinguishing the faint starlight reflected by such planets from the far brighter signal anticipated from any exozodiacal dust. When these results are extrapolated out into the asteroid belt, the total mass of the light–reflecting asteroidal dust component is at most $\sim 2.3 \times 10^{18}$ gm. Note that this mass–limit is also contaminated by dust from JFCs, and it corresponds to an asteroid that is at most ~ 12 km across.

When these results are extrapolated out to Oort Cloud distances of $a \sim 10^4$ AU, the inferred mass of Oort Cloud dust is $\sim 10^{19}$ gm (but uncertain by orders of magnitude), which is equivalent to a 30 km comet. This dust is ultimately stripped from the Sun by the interstellar gas and dust that flows around and through the solar system. This then suggests that the Sun, and perhaps also other stars having cometary Oort Clouds, each have vast but tenuous stellar dust tails that are oriented in the downstream direction of the local interstellar flows.

A. Appendix A

To relate a pixel's (x, y) coordinates to the right ascension and declination (α, δ) it subtends on the sky, place a Cartesian coordinate system with its origin at the center of the lens with the $\hat{\mathbf{x}}$, $\hat{\mathbf{y}}$ axes parallel to the CCD's rows and columns (see Fig. 1). The $\hat{\mathbf{z}}$ axis is the camera's optical axis which intercepts the CCD at the pixel having coordinates $(x_o, y_o) = (191, 286)$. Let the vector $\mathbf{r}_\star$ point to a star having angular coordinates (θ, ϕ); these will be called the lens coordinates. In cartesian (x, y, z) components, the star's lens coordinates are $\mathbf{r}_\star = (R \sin \phi \cos \theta, R \sin \theta, R \cos \phi \cos \theta)$, and the length of this vector is chosen to be the lens radius R. An image of this star also forms at the back side of the lens at $-\mathbf{r}_\star$. Fig. 1 shows that the fiber optic pipes this starlight to a spot on the CCD that lies a distance X away from the optical axis in the $\hat{\mathbf{x}}$ direction and Y away in the $-\hat{\mathbf{y}}$ direction. Note that the orientation of the X and Y axes are chosen to point in the customary manner such that when $\hat{\mathbf{y}}$ points to equatorial north, the $+Y$ direction is north and the $+X$ direction is west. If l is the physical size of a pixel, then $X = l(x - x_o) = -\mathbf{r}_\star \cdot \hat{\mathbf{x}}$, $Y = l(y - y_o) = \mathbf{r}_\star \cdot \hat{\mathbf{y}}$, and

$$x - x_o = -\sin \phi \cos \theta / p \tag{A1a}$$
$$y - y_o = \sin \theta / p \tag{A1b}$$

relates the star's (x, y) coordinates on the CCD to its lens coordinates (θ, ϕ). The plate–scale $p = \ell / R$ is simply the ratio of the pixel width to the lens radius, and is also the angle subtended by the pixel at the optical axis.

Now relate the lens coordinates (θ, ϕ) to equatorial coordinates (α, δ). Suppose the optical axis $\hat{\mathbf{z}}$ points to right ascension α_o and declination δ_o, and the $\hat{\mathbf{y}}$ axis differs from equatorial north by a rotation about the $\hat{\mathbf{z}}$ axis by angle τ. This angle is the position angle of equatorial north, and on the CCD it is measured from the Y axis towards the east. In this coordinate system the star's cartesian components are $\mathbf{r}_\star(\alpha, \delta) = (R \sin \alpha \cos \delta, R \sin \delta, R \cos \alpha \cos \delta)$ when expressed in terms of its equatorial coordinates. It is straightforward to show that this star's position vector $\mathbf{r}_\star(\alpha, \delta)$ in equatorial coordinates can be obtained from the its position vector in lens coordinates $\mathbf{r}_\star(\phi, \theta)$ after performing the following rotations upon the lens coordinate system:

$$\mathbf{r}_\star(\alpha, \delta) = \mathcal{R}_y(-\alpha_o) \mathcal{R}_x(\delta_o) \mathcal{R}_z(-\tau) \mathbf{r}_\star(\theta, \phi) \tag{A2}$$

where $\mathcal{R}_i(\omega)$ is the matrix that rotates a right–handed coordinate system about axis i by angle ω. Performing the rotations and equating the (x, y, z) components in Eq. (A2) yields the relationship between a pixel's lens coordinates (θ, ϕ) and its equatorial coordinates (α, δ):

$$\sin \delta = g \cos \delta_o + h \sin \delta_o \tag{A3a}$$
$$\tan \alpha = \frac{k \sin \alpha_o + f \cos \alpha_o}{k \cos \alpha_o - f \sin \alpha_o} \tag{A3b}$$

where f, g, h, and k are shorthand for

$$f = \cos \tau \sin \phi \cos \theta - \sin \tau \sin \theta \tag{A4a}$$

$$g = \sin\tau\sin\phi\cos\theta + \cos\tau\sin\theta \tag{A4b}$$

$$h = \cos\phi\cos\theta \tag{A4c}$$

$$k = h\cos\delta_o - g\sin\delta_o. \tag{A4d}$$

Next, get the star's geocentric ecliptic longitude and latitude (Λ, Θ) where $\mathbf{r}_\star(\Lambda, \Theta) = (R\sin\Lambda\cos\Theta, R\sin\Theta, R\cos\Lambda\cos\Theta)$. These are obtained by rotating the ecliptic coordinates about the z axis by the Earth's obliquity $\sigma = 23.4393°$, *i.e.*, $\mathbf{r}_\star(\Lambda, \Theta) = \mathcal{R}_z(\sigma)\mathbf{r}_\star(\alpha, \delta)$. Equating cartesian components yields

$$\sin\Theta = \cos\sigma\sin\delta - \sin\sigma\sin\alpha\cos\delta \tag{A5a}$$

$$\tan\Lambda = \frac{\cos\sigma\sin\alpha\cos\delta + \sin\sigma\sin\delta}{\cos\alpha\cos\delta}. \tag{A5b}$$

This gives the star's longitude measured from the vernal equinox. To get the star's longitude relative to the Sun, use Eq. (A5b) to compute the Sun's longitude $\Lambda_\odot$ and form the difference $\Lambda - \Lambda_\odot$.

The observed angular separation Φ_{01} between two known stars can be used to determine the detector's plate–scale p. If the stars have lens coordinates (θ_0, ϕ_0) and (θ_1, ϕ_1), which depend on p, and equatorial coordinates (α_0, δ_0) and (α_1, δ_1), then spherical geometry gives their angular separation:

$$\cos\Phi_{01} = \cos\theta_0\cos\theta_1\cos(\phi_0 - \phi_1) + \sin\theta_0\sin\theta_1 \tag{A6a}$$

$$= \cos\delta_0\cos\delta_1\cos(\alpha_0 - \alpha_1) + \sin\delta_0\sin\delta_1. \tag{A6b}$$

This equation can be solved for p when coupled with Eqs. (A1). Another useful quantity is the angular separation between star 0 and the optical axis at $(\theta_1, \phi_1) = (0, 0)$,

$$\cos\Phi_0 = \cos\theta_0\cos\phi_0. \tag{A7}$$

Using Fig. 1, it can also be shown that an off–axis pixel subtends a larger solid angle $\Omega(\Phi_0)$ than the on–axis pixel:

$$\frac{\Omega}{\Omega_0} = \frac{1}{\cos\Phi_0} \tag{A8}$$

where $\Omega_0 = p^2$ is the solid angle of the pixel at the optical axis. For example, a pixel in the CCD corner at $\Phi_0 = 25°$ sees a solid angle that is 10% larger than the on–axis pixel.

B. Appendix B

Flatfield data for camera B were acquired prior to launch in a laboratory at Research Support Instruments, which is the subcontractor that integrated the star trackers into the Clementine

payload. These images were acquired with star tracker B exposed to an integrating sphere, which is a spherical light source having a uniform radiance. The averaged image acquired in the lab is shown in Fig. 16A. The following describes several problems in these data, as well as the procedures used to construct the star tracker flatfield from these data.

(i.) The integrating sphere was too bright to produce unsaturated images at the star tracker's shortest possible exposure time. To get unsaturated images, a Wrattan neutral density ND2 filter was placed in front of the camera. It is thus conceivable that if there are any spatial variations $\delta T(x, y)$ in this filter's transmission coefficient $T(x, y)$, the resulting flatfielded data would then exhibit fractional errors $\delta T/T$. However we have ruled out this possibility by examining distinct yet overlapping zodiacal light fields acquired during different orbits with different camera orientations. In every case, the photometry in each overlapping, flatfielded image was self–consistent. This indicates that any errors $\delta T(x, y)$ that may have been introduced into the flatfield by the use of the neutral density filter are negligible.

(ii.) The dark current was not measured when the flatfield data were acquired. This could have been quite problematic since the the subtraction of the dark current has a dramatic affect upon the brightness of the flatfield center relative to its edges (see Fig. 16). However a good flatfield is still recoverable due to the fortunate presence of the five round blemishes seen in Fig. 16. These blemishes correspond to a $\sim 10\%$ decrease in the camera's sensitivity, and their cause is unknown. These blemishes are present in all of the raw zodiacal light images acquired by star tracker B (*c.f.* the lower right corner of Fig. 4A). However the relative depth of the blemish increases with increasing dark current d, so it is straightforward to find the appropriate value for d that yields a flatfield that removes the blemishes from all of the zodiacal light images. Note that the flatfielded image in Fig. 4B does not exhibit these blemishes.

(iii.) Vignetting by the mount that secured the neutral density filter to the camera also darkened the outer edges of the flatfield data (see Fig. 16A). Interior to the vignetted region, the flatfield's surface brightness empirically varies as a simple polynomial

$$\mathrm{flat}(x, y) = 1 - 1.95\Phi_0^2(x, y) \tag{B1}$$

that is a function of the angular distance Φ_0 of pixel (x, y) from the the optical axis (see Eq. A7). In order to reconstruct the flatfield at the edges, Eq. (B1) is extrapolated into the vignetted region at $\Phi_0 > 20°$, which results in the flatfield shown in Fig. 16B. Gaussian noise is also added to the extrapolated region in amounts comparable to that seen just interior.

The pixel–to–pixel variations seen over short spatial scales in Fig. 16 is simply photon–counting noise—they do not represent real changes in the camera's sensitivity. This becomes evident when flatfielding these images. Ordinarily, flatfielding an image makes it look 'cleaner' since the pixel–to–pixel variations in the CCD's sensitivity are removed from the image. However the application of the flatfield seen in Fig. 16B actually makes the zodiacal light images look a little bit noisier. It may be concluded that the short–wavelength variations seen in the flatfield are simply noise, and that we are justified in adding gaussian noise to the extrapolated parts of the flatfield. (Failure to

add this noise creates a lower–noise zone at the edge of a flatfielded image having a very artificial appearance.) The standard deviation of this noise near the optical axis is about 2% of the flatfield's surface brightness, and it increases to about 7% at the edge.

Figure 16 and Eq. (B1) show that the surface brightness of the flatfield decreases with distance from the optical axis by as much as 40% at the CCD corners where $\Phi_0 = 25°$. This seemingly runs contrary to expectations since Appendix A shows that pixels further from the optical axis subtend a solid angle that is larger by a factor of $1/\cos(\Phi_0)$ (Eq. A8), and perhaps should be brighter. However this effect is more than offset by transmission inefficiencies in the fiber–optic and also vignetting by the lens housing, both of which get more severe for light entering the lens at larger angles (Lewis *et al.* 1991). Consequently, dividing a raw image by this flatfield simultaneously corrects for two effects: it compensates for the camera's reduced detection efficiency at higher Φ_0 as well as for the pixels' larger solid angle.

Because the reconstructed flatfield of Fig. 16B compensates for a pixel's larger solid at higher Φ_0, it should only be used when doing photometry on distributed sources such as the zodiacal light. But if photometry on point–sources is desired, a "point–source" flatfield, which is just Fig. 16B $\times \cos(\Phi_0)$, must instead be used to flatfield the images.

The observed intensity of several stars imaged during orbit 66 are used to test this reconstructed flatfield. The spacecraft was maneuvering while this image sequence was acquired, so stars seen in different images wander across the field. Figure 17 plots the normalized intensity of five bright stars seen in different images versus their angular distance Φ_0 from the optical axis. The grey curves are their intensities prior to flatfielding, which shows how the camera's detection efficiency drops with Φ_0. The black curves shows the intensities of these stars when the point–source flatfield is used. This test demonstrates that when the reconstructed flatfield is used, the stars' intensities are constant when imaged at different position on the CCD, as they should.

REFERENCES

Aller, L. H., G. Duffner, M. Dworetsky, D. Gudehus, S. Kilston, D. Leckrone, J. Montgomery, J. Oliver, and E. Zimmerman 1967. Some models of the zodiacal cloud. In *The Zodiacal Light and the Interplanetary Medium* (J. L. Weinberg, Ed.), pp. 243–256. NASA–SP 150.

Brown, M. E. 2001. The inclination distribution of the Kuiper Belt. *AJ*, **121**, 2804–2814.

Brownlee, D. E., D. J. Joswiak, S. G. Love, A. O. Nier, D. J. Schlutter, and J. P. Bradley 1993. Identification of cometary and asteroidal particles in stratospheric IDP collections. *Lunar and Planetary Sci. XXIV*, 205.

Dermott, S. F., P. D. Nicholson, J. A. Burns, and J. R. Houck 1984. Origin of the solar system dust bands discovered by IRAS. *Nature*, **312**, 505–509.

Dermott, S. F., D. D. Durda, B. Å. S. Gustafson, S. Jayaraman, J.–C. Liou, and Y.–L. Xu 1994. Modern sources of dust in the solar system. In *Workshop on the Analysis of Interplanetary Dust Particles* (M. Zolensky, Ed.), Lunar and Planetary Inst. Technical Report 94–02, pp. 17–18.

Dermott, S. F., K. Grogan, D. D. Durda, S. Jayaraman, T. J. J. Kehoe, S. J. Kortenkamp, and M. C. Wyatt 2001. Orbital evolution of interplanetary dust. In *Interplanetary Dust* (E. Grün, B. Å. S. Gustafson, S. F. Dermott, and H. Fechtig, Eds.), Springer–Verlag, Berlin, p. 569.

Divari, N. B. 1968. A meteor model for the zodiacal cloud. *Soviet Physics–Astronomy*, **11**, 1048–1052.

Divine, N. 1993. Five populations of interplanetary meteoroids. *J. Geophys. Res.*, **98**, 17029–17048.

Duncan, M., T. Quinn, and S. Tremaine 1987. The formation and extent of the solar system comet cloud. *AJ*, **94**, 1330–1338.

Frisch, P. C. 2000. The galactic environment of the Sun. *J. Geophys. Res.*, **105**, 10279–10289.

Giese, R. H. and C. V. Dziembowski 1969. Suggested zodiacal light measurements from space probes. *Planet. Space Sci.*, **17**, 949–956.

Grogan, K., S. F. Dermott, and D. D. Durda 2001. The size–frequency distribution of the zodiacal cloud: evidence from the solar system dust bands. *Icarus*, **152**, 251–267.

Grün, E., H. A. Zook, H. Fechtig, and R. H. Giese 1985. Collisional balance of the meteoritic complex. *Icarus*, **62**, 244–272.

Grün, E., P. Staubach, M. Baguhl, D. P. Hamilton, H. A. Zook, S. Dermott, B. A. Gustafson, H. Fechtig, J. Kissel, D. Linkert, G. Linkert, R. Srama, M. S. Hanner, C. Polanskey, M. Horanyi, B. A. Lindblad, I. Mann, J. A. M. McDonnell, G. E. Morfill, and G. Schwehm

1997. South–north and radial traverses through the interplanetary dust cloud. *Icarus*, **129**, 270–288.

Hanner, M. S., J. L. Weinberg, L. M. Shields II, B. A. Green, and G. N. Toller 1974. Zodiacal light in the asteroid belt: the view from Pioneer 10. *J. Geophys. Res.*, **79**, 3671–3675.

Hong, S. S. 1985. Henyey–Greenstein representation of the mean volume scattering phase function for zodiacal dust. *A&A*, **146**, 67–75.

Jackson, A. A. and H. A. Zook 1992. Orbital evolution of dust particles from comets and asteroid. *Icarus*, **97**, 70–84.

Kelsall, T., J. L. Weiland, B. A. Franz, W. T. Reach, R. G. Arendt, E. Dwek, H. T. Freudenreich, M. G. Hauser, S. H. Moseley, N. P. Odegard, R. F. Silverberg, E. L. Wright 1998. The COBE diffuse infrared background experiment search for the cosmic infrared background. II. Model of the interplanetary dust cloud. *ApJ*, **508**, 44–73.

Kordas, J. F., I. T. Lewis, B. A. Wilson, D. P. Nielsen, H. S. Park, R. E. Priest, R. F. Hills, M. J. Shannon, A. G. Ledebuhr, and L. D. Pleasance 1995. The star tracker stellar compass for the Clementine mission. *Proc. SPIE*, **2466**, 70–83.

Lamy, P. L. and J.–M. Perrin 1986. Volume scattering function and space distribution of the interplanetary dust cloud. *A&A*, **163**, 269–286.

Leinert, C. 1975. Zodiacal light—a measure of the interplanetary environment. *Space Sci. Rev.*, **18**, 281–339.

Leinert, C., M. Hanner, I. Richter, and E. Pitz 1980. The plane of symmetry of interplanetary dust in the inner solar system. *A&A*, **82**, 328–336.

Leinert, C., I. Richter, E. Pitz, and B. Planck 1981. The zodiacal light from 1.0 to 0.3 A.U. as observed by the Helios space probes. *A&A*, **103**, 177-188.

Leinert, Ch., S. Bowyer, L. H. Haikala, M. S. Hanner, M. G. Hauser, A.-Ch. Levasseur-Regourd, I. Mann, K. Mattila, W. T. Reach, W. Schlosser, H. J. Staude, G. N. Toller, J. L. Weiland, J. L. Weinberg, and A. N. Witt 1998. The 1997 reference of diffuse night sky brightness. *Astron. Astrophys. Suppl. Ser.*, **127**, 1-99.

Lester, T. P., M. L. McCall, and J. B. Tatum 1979. Theory of planetary photometry. *JRASC*, **73**, 233–257.

Levison, H. F. and M. J. Duncan 1997. From the Kuiper Belt to Jupiter–family comets: the spatial distribution of ecliptic comets. *Icarus*, **127**, 13–32.

Levison, H. F., L. Dones, and M. J. Duncan 2001. The origin of Halley–type comets: probing the inner Oort cloud. *AJ*, **121**, 2253–2267.

Lewis, I. T., A. G. Ledebuhr, T. S. Axelrod, J. F. Kordas, and R. F. Hills 1991. Wide–field–of–view star tracker camera. *Proc. SPIE*, **1478**, 2–12.

Liou, J. C., S. F. Dermott, and Y. L. Xu 1995. The contribution of cometary dust to the zodiacal cloud, *Planet. Space Sci.*, **43**, 717–722.

Marsden, B. G. and G. V. Williams 1999. *Catalogue of Cometary Orbits*, 13th ed. Central Bureau for Astronomical Telegrams and Minor Planet Center, Smithsonian Astrophysical Observatory, MA.

Neugebauer, G., C. A. Beichman, B. T. Soifer, H. H. Aumann, T. J. Chester, T. N. Gautier, F. C. Gillett, M. G. Hauser, J. R. Houck, C. J. Lonsdale, F. J. Low, and E. T. Young 1984. Early results from the Infrared Astronomical Satellite. *Science* , **224**, 14–21.

Reach, W. T., B. A. Franz, and J. L. Weiland 1997. The three–dimensional structure of the zodiacal dust bands. *Icarus*, **127**, 461–484.

Weissman, P. R. 1996. In *Completing the Inventory of the Solar System*, (T. W. Rettig and J. M. Hahn, Eds.), pp. 265–288, *ASP Conference Series*, **107**.

Whipple, F. L. 1955. A comet model. III. The zodiacal light. *ApJ*, **121**, 750–770.

Whipple, F. L. 1967. On maintaining the meteoritic complex. In *Zodiacal Light and the Interplanetary Medium*, (J. L. Weinberg, Ed.), NASA SP–150, pp. 409–425.

Wyatt, M. C., S. F. Dermott, C. M. Telesco, R. S. Fisher, K. Grogan, E. K. Holmes, and R. K. Pia 1999. How observations of circumstellar disk asymmetries can reveal hidden planets: pericenter glow and its application to the HR 4796 disk. *ApJ*, **527**, 918–944.

Zook, H. A., B. L. Cooper, and A. E. Potter 1997. The zodiacal light as observed with the Clementine startracker cameras: calibration and image analysis procedures. *Lunar and Planetary Science XXVIII*, abstract #1103.

Table I.   Zodiacal Light Observations

Orbit number	Date (1994)	Ecliptic longitude (degrees)	Total exp. time (seconds)
66	March 5.9	345.1	2.6
110	March 15.0	354.2	0.3
110	March 15.0	354.3	0.6
164	March 26.4	5.5	8.7
193	April 1.5	11.5	11.6
206	April 4.0	14.0	11.4
253	April 13.9	23.7	13.9

Table II.   Parameters for the Best Fit

j	ν_j	f_j
low	1.00	0.45 ± 0.13
high	1.45	0.50 ± 0.02
iso	2.00	0.05 ± 0.02
$a\sigma_1 r_1 = (7.4 \pm 1.8) \times 10^{-9}$		
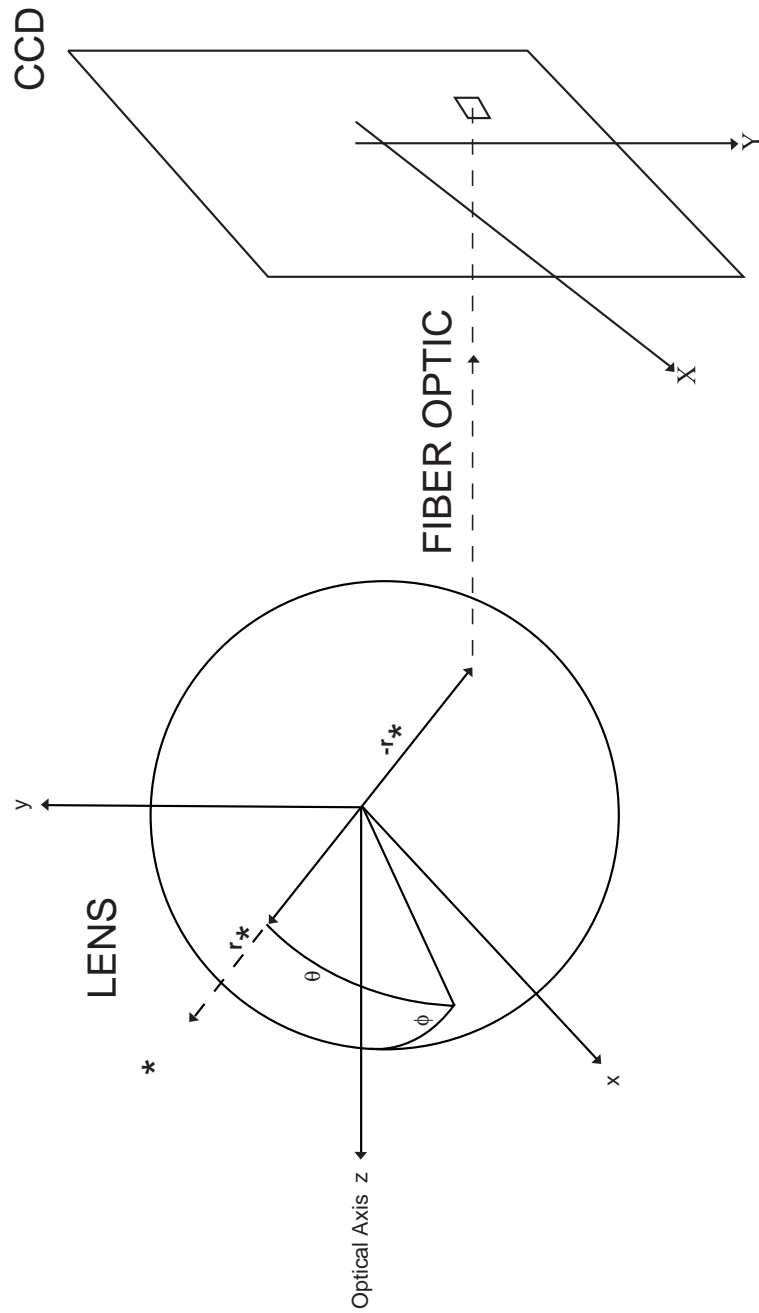
Fig. 1.— A schematic of the star tracker camera which has three principle components: a spherical lens and a fiber optic that pipes light from the backside of the lens to the CCD detector.
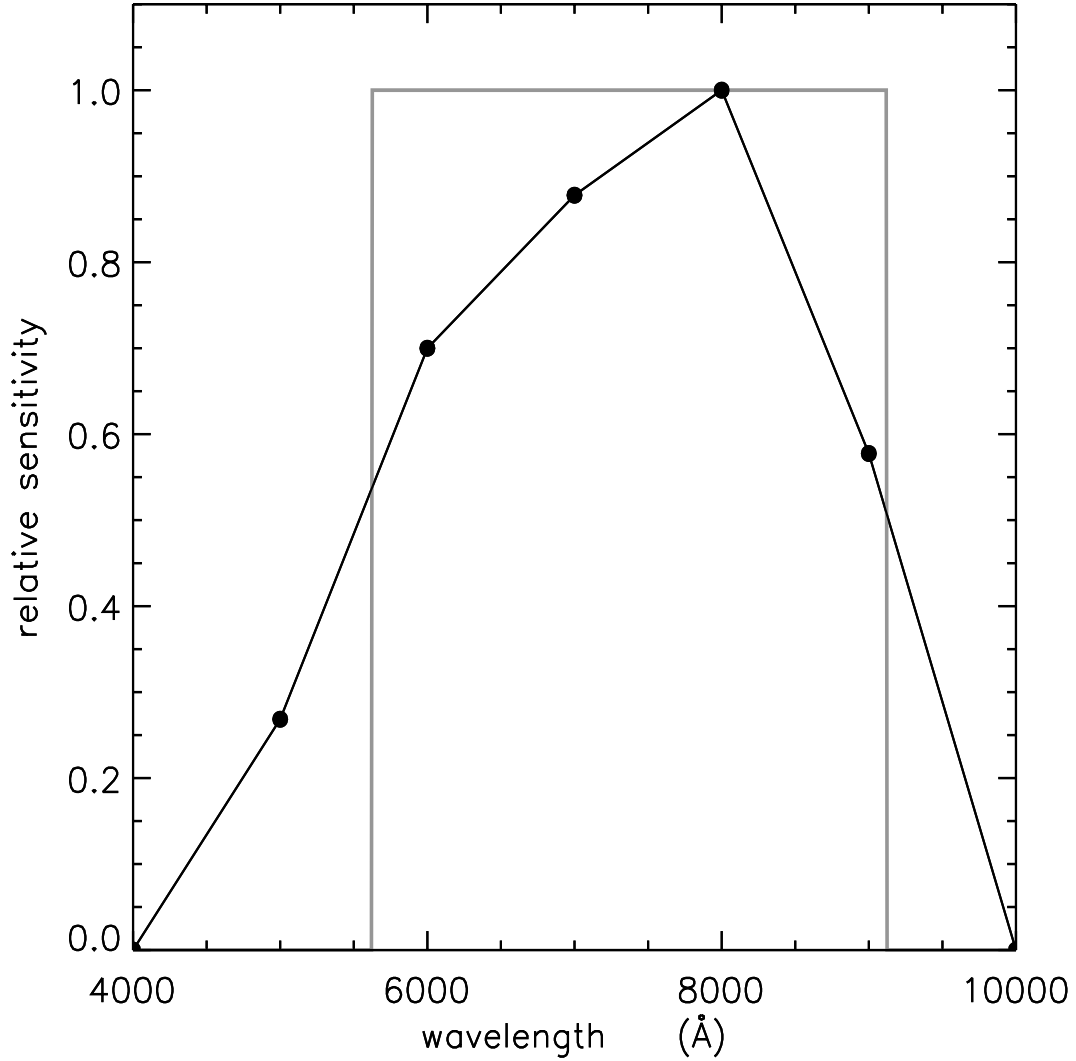
Fig. 2.— The dots indicate the relative sensitivity of the star tracker camera to light of discrete wavelengths of $\lambda = 5000$ to 9000 Å sampled over 1000 Å intervals; these data are provided by J. F. Kordas (private communication). The dark curve simply connects the dots and also assumes that the camera sensitivity is zero at $\lambda = 4000$ and $\lambda = 10000$ Å. The grey box is an equivalent square bandpass.
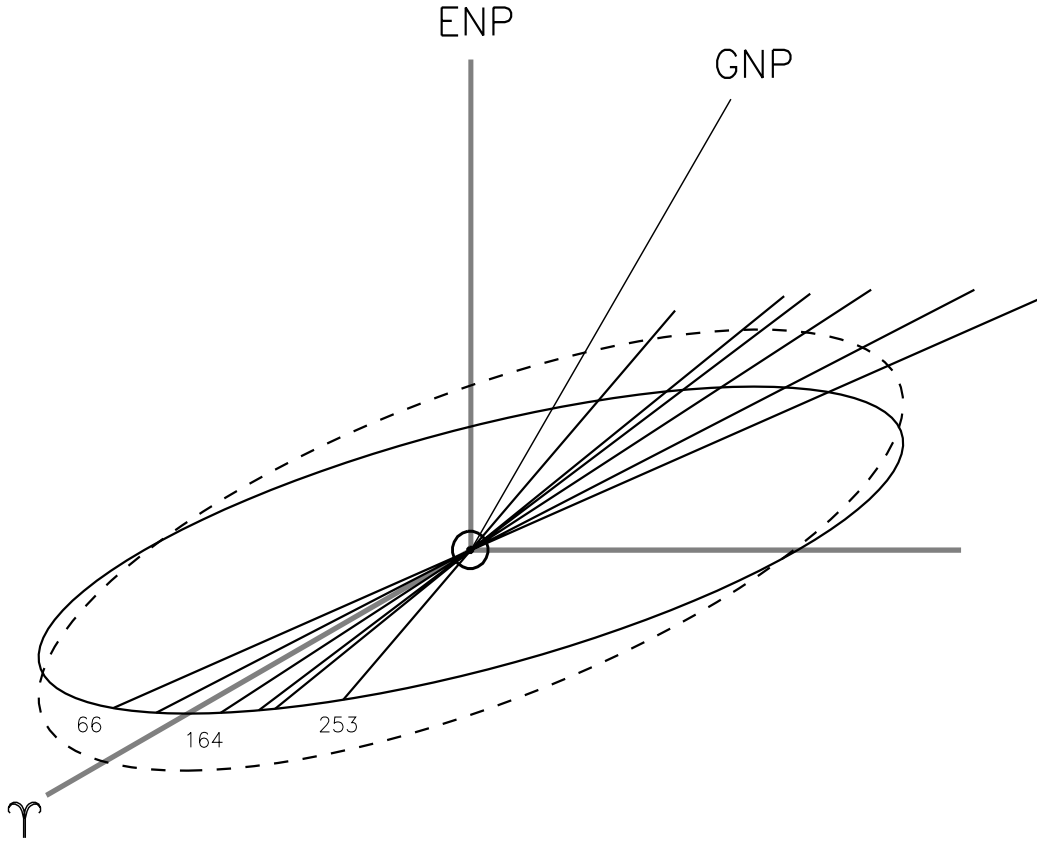
Fig. 3.— The narrow lines show the heliocentric ecliptic longitudes of the spacecraft's lines–of–sight through the inner zodiacal light, a few of which are labeled by their orbit number (see Table I). Longitudes are measured counter–clockwise from the direction of the vernal equinox γ. The dark ellipse is Earth's orbit about the Sun $\odot$ with ENP indicating the ecliptic north pole. The dashed circle represents the $i = 3°$ tilt of the zodiacal light's midplane which has a longitude of ascending node $\Omega = 87°$ (Leinert *et al.* 1980). The galactic north pole GNP is also indicated, and it has an heliocentric ecliptic longitude $\lambda_g = 180.0°$ and latitude $\beta_g = 29.8°$.
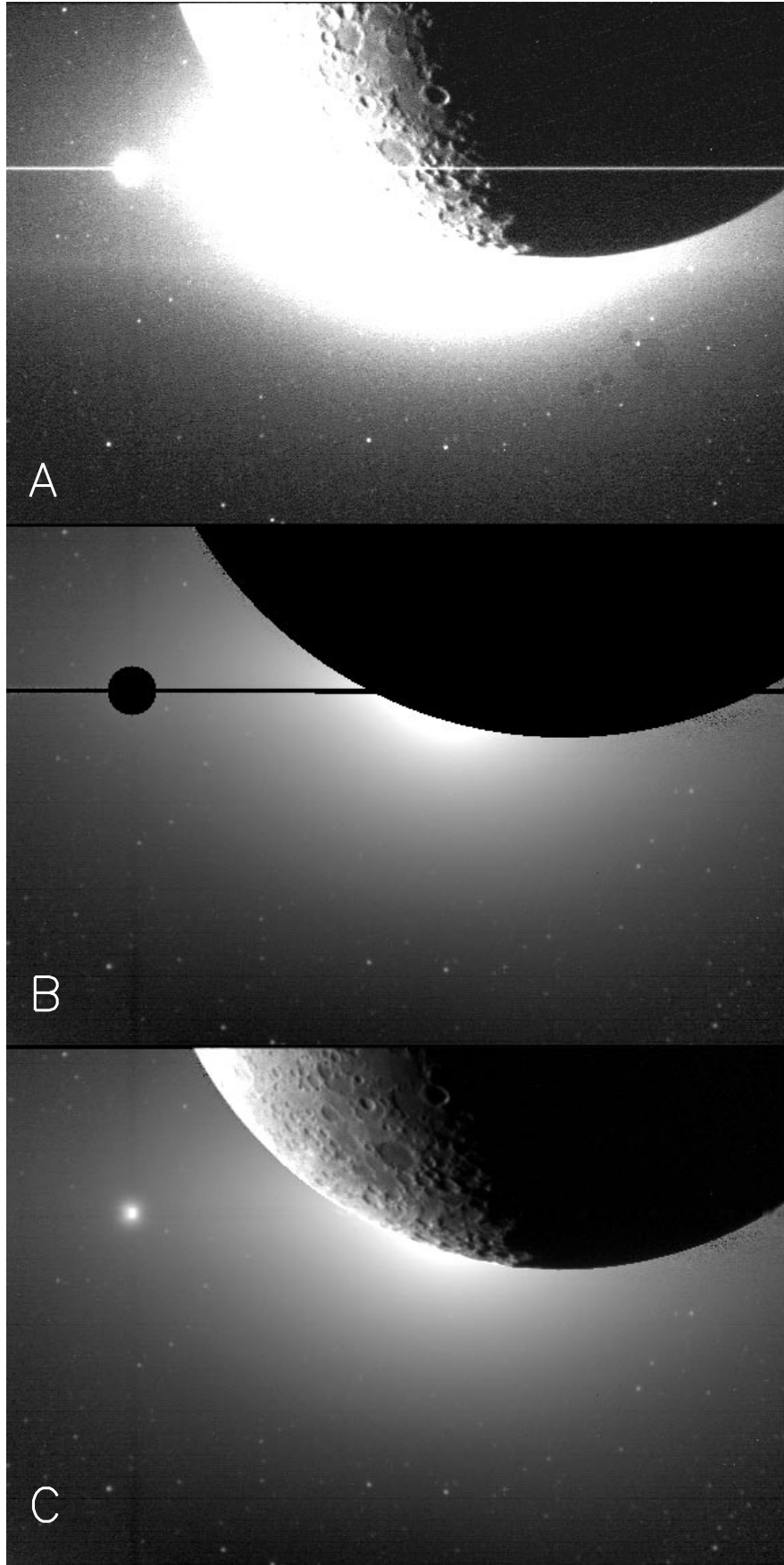
Fig. 4.— Star tracker images shown at different stages of analysis. **A**. A typical raw star tracker image acquired during a 0.4 sec exposure in orbit 193. We saturate this linear greyscale at a surface brightness of 4×10^{-12} B$_\odot$ in order to reveal the faint artifacts present in the data. The CCD's columns run left–right and ecliptic north/east are approximately up/left. The bright object left of the Moon is a saturated Venus whose signal has bled into the adjacent pixels. **B**. This logarithmic greyscale shows the master image for orbit 193 in the surface brightness interval $4 \times 10^{-13} < Z < 8 \times 10^{-11}$ B$_\odot$. **C**. This cosmetically enhanced master has had its data–gaps filled in with images of the Moon and Venus.
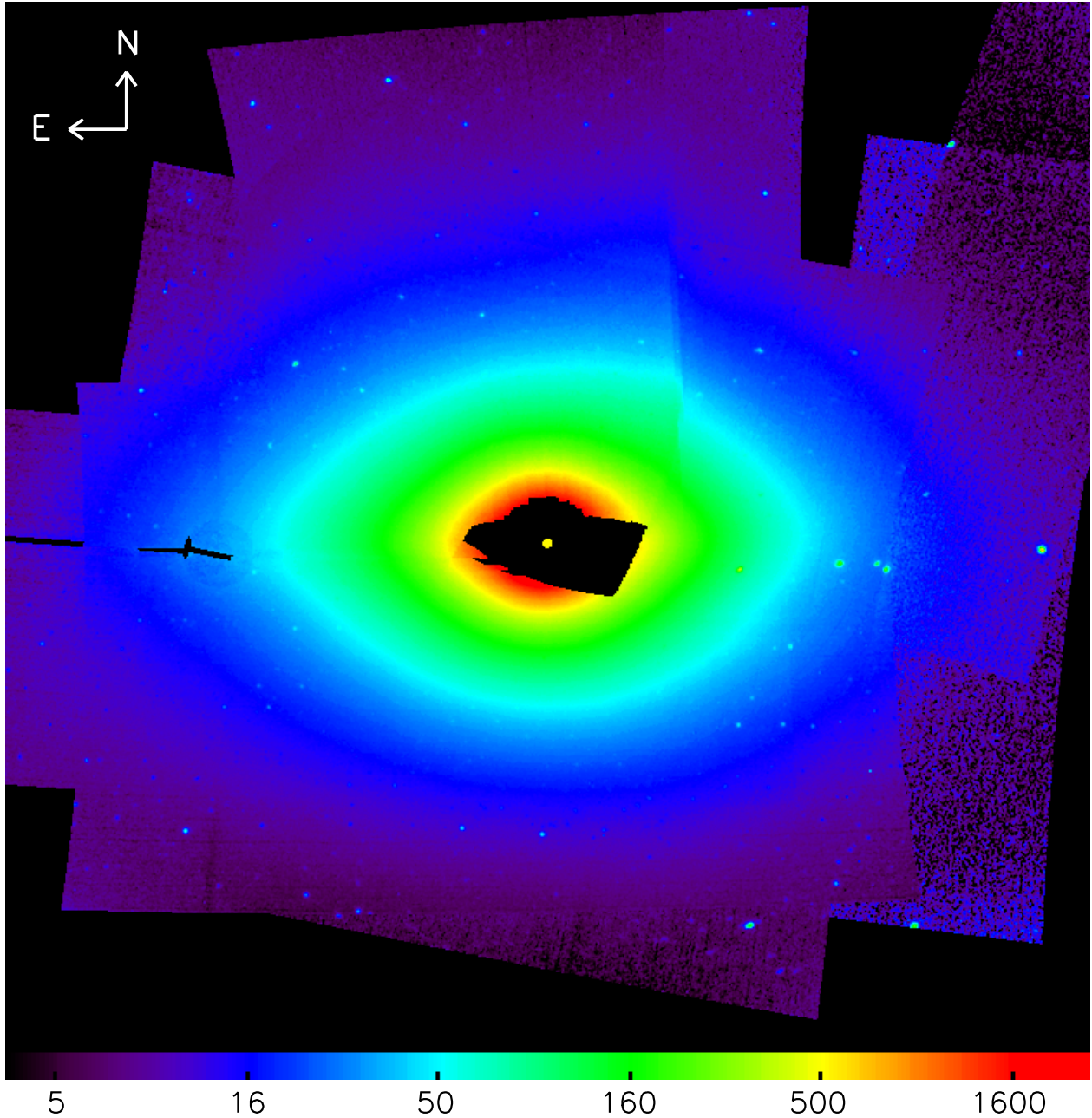
Fig. 5.— A mosaic of seven fields of the inner zodiacal light observed by the Clementine star tracker camera. The colorbar indicates surface brightness in units of $10^{-13}B_\odot$. Ecliptic north and east are up and left in this mercator projection, and the field of view is $60 \times 60°$. Black indicates gaps in the data, and the Sun is drawn to scale at the center of the mosaic. Regions beyond $\Phi \sim 10°$ northwest of the Sun are polluted by scattered light, and the "dimple" $20°$ east of the Sun is a lower signal/noise patch that was polluted by Venus.
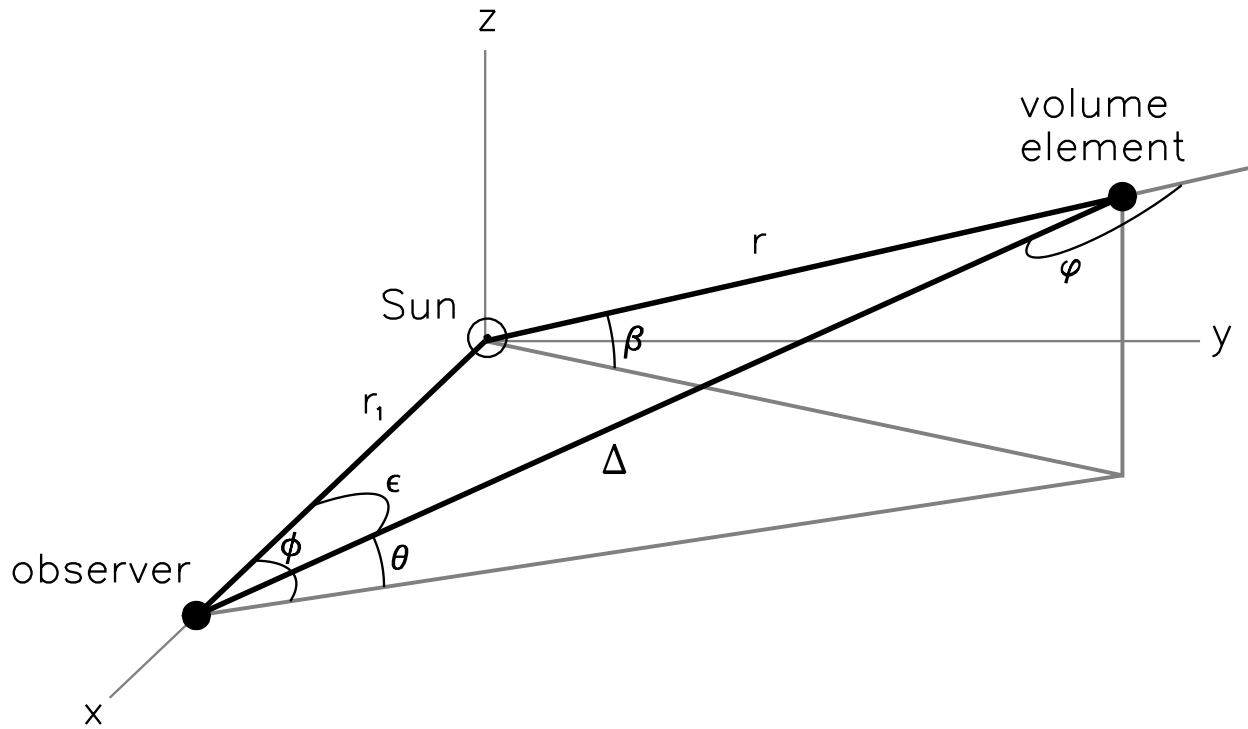
Fig. 6.— The viewing geometry for light scattered by a dust volume element a distance r from the Sun at heliocentric latitude β measured from the ecliptic x–y plane. The observer has a heliocentric distance r_1 and the line–of–sight (LOS) to the volume element a distance Δ away has a geocentric latitude θ, longitude ϕ, and an elongation angle ϵ measured from the sunward direction. The scattering angle φ is measured from the LOS to the anti–solar direction at the volume element.
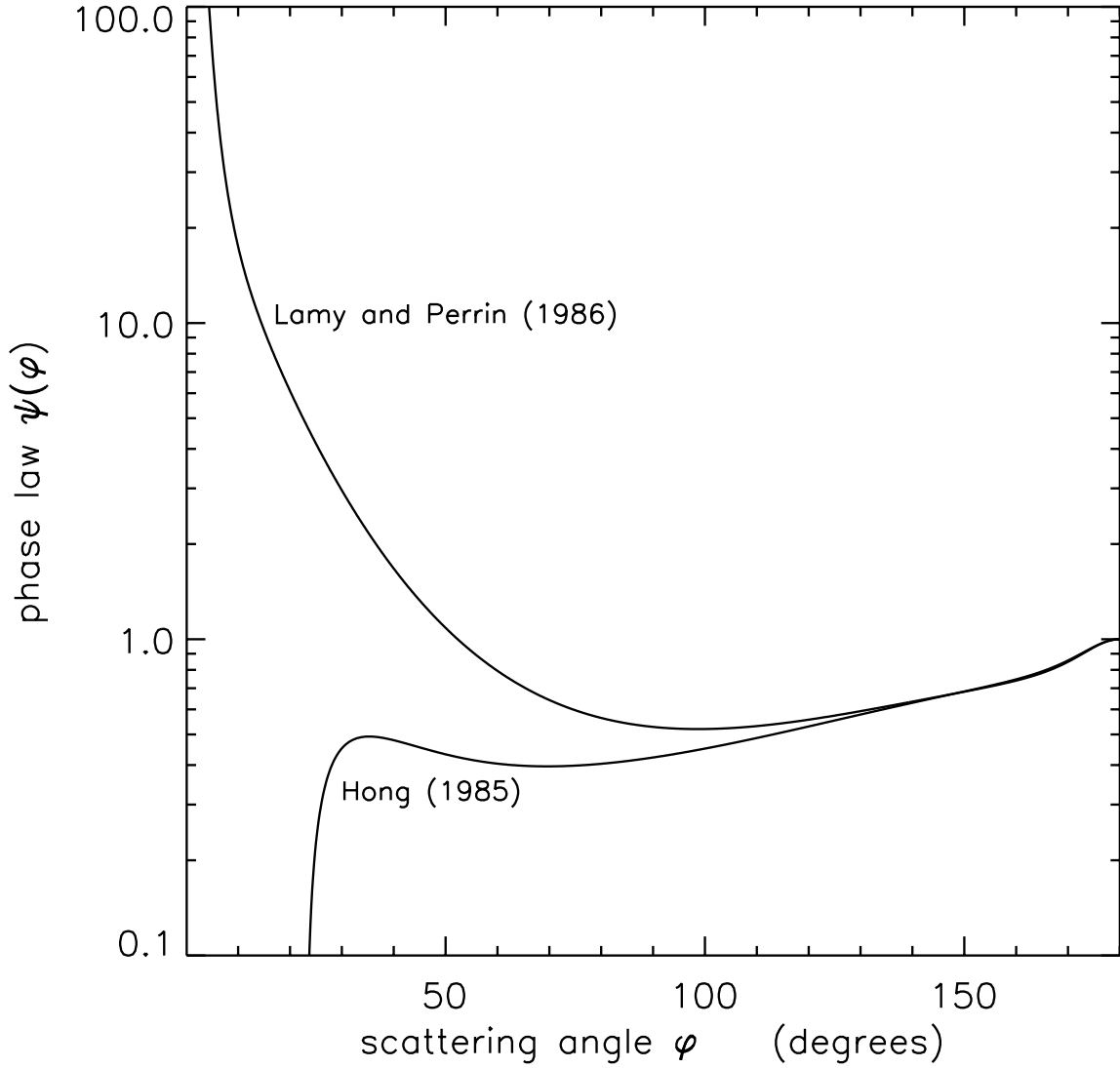
Fig. 7.— The upper curve is the phase law obtained from the nominal volume scattering function of Lamy and Perrin (1986), while the lower curve is from Hong (1985). Note that the phase laws shown here are simply the volume scattering functions with the dust albedo a and cross sectional density σ_1 factored out and normalized to unity at $\varphi = \pi$ where the phase angle $\pi - \varphi = 0$. Although Hong (1985) gives a phase law for a $\nu = 1$ radial power law, we have used his Eqns. (10) and (14) to form the phase law shown here that is appropriate for a $\nu = 1.45$ dust distribution.
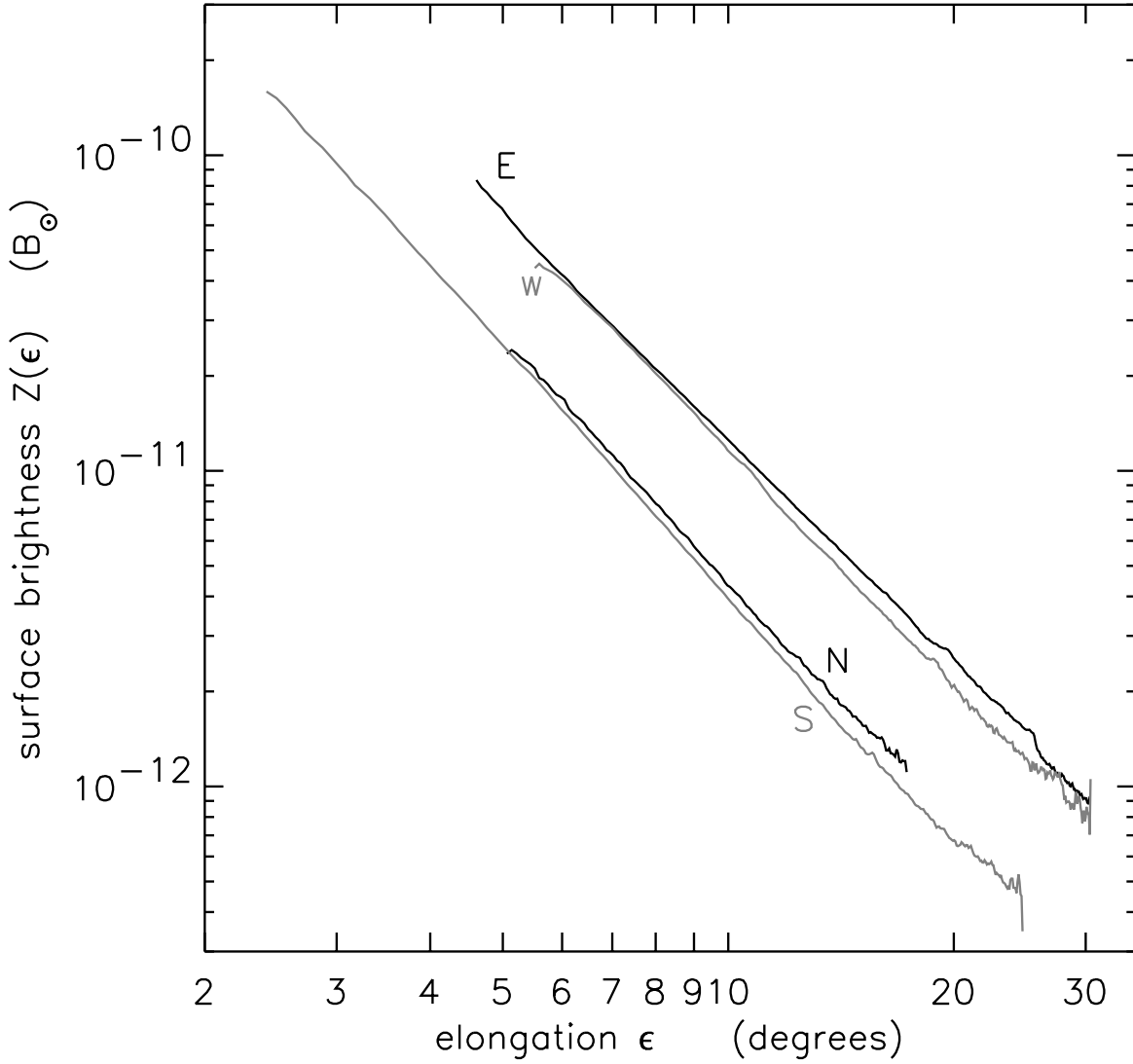
Fig. 8.— The surface brightness of the zodiacal light mosaic of Fig. 5 is plotted versus elongation angle ϵ. Each profile is computed in a 10 degree–wide triangular aperture oriented North, South, East, or West of the Sun. The light–polluted field acquired during orbit 164 (which lies north of the Sun) is discarded before generating these profiles, as are pixels that subtend data–gaps, bright stars, or planets.
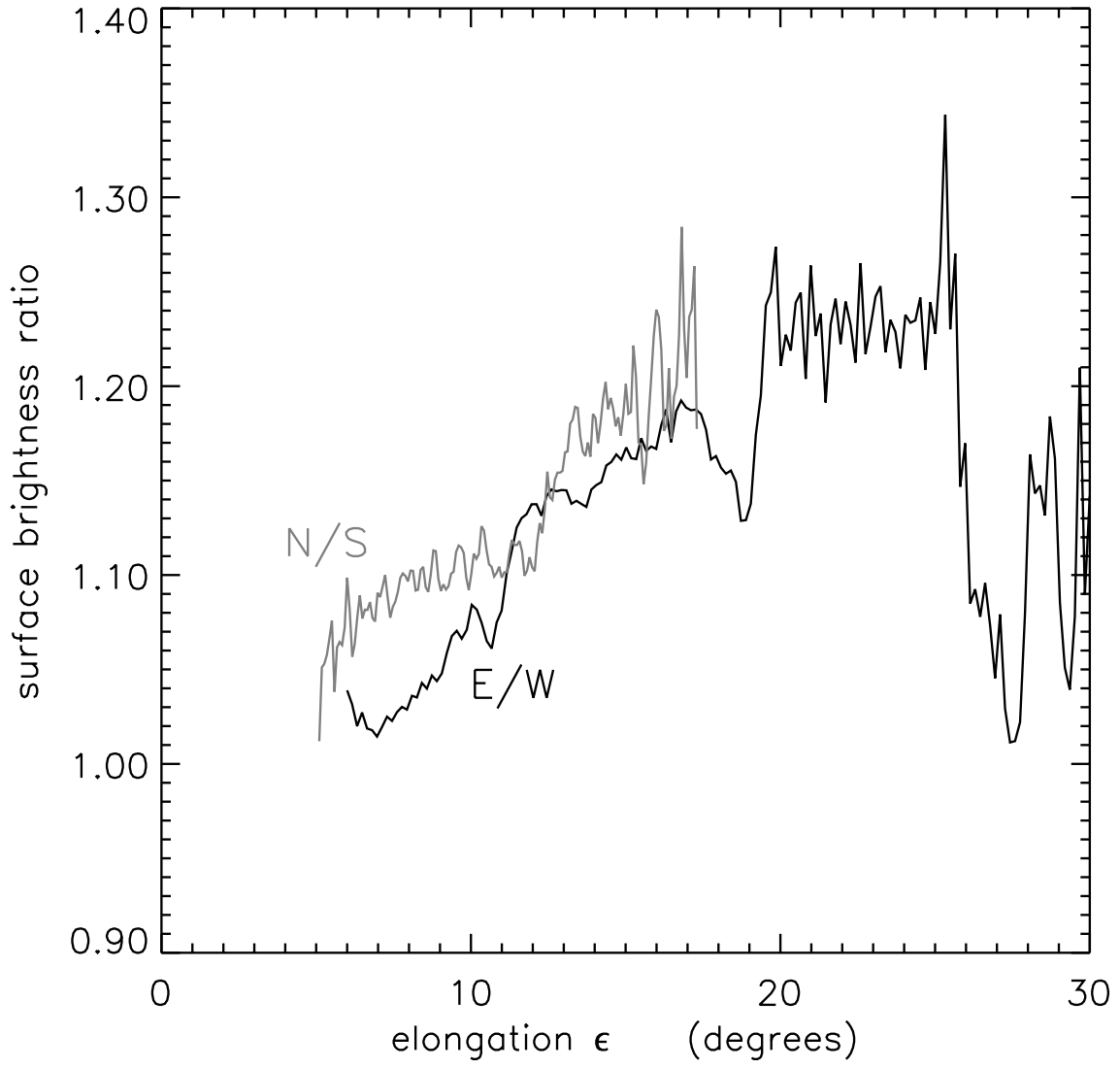
Fig. 9.— Ratios of the brightness profiles of Fig. 8 are plotted versus elongation angle ϵ, where N/S and E/W indicate the north/south and east/west ratios.
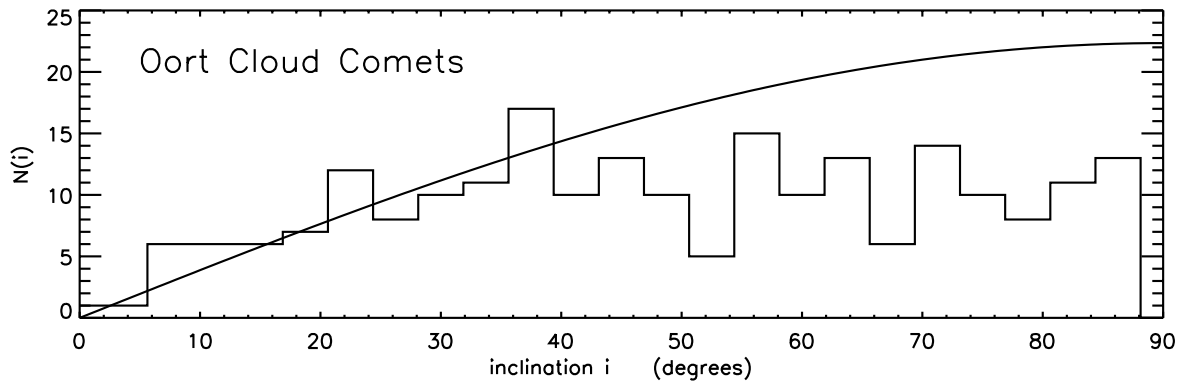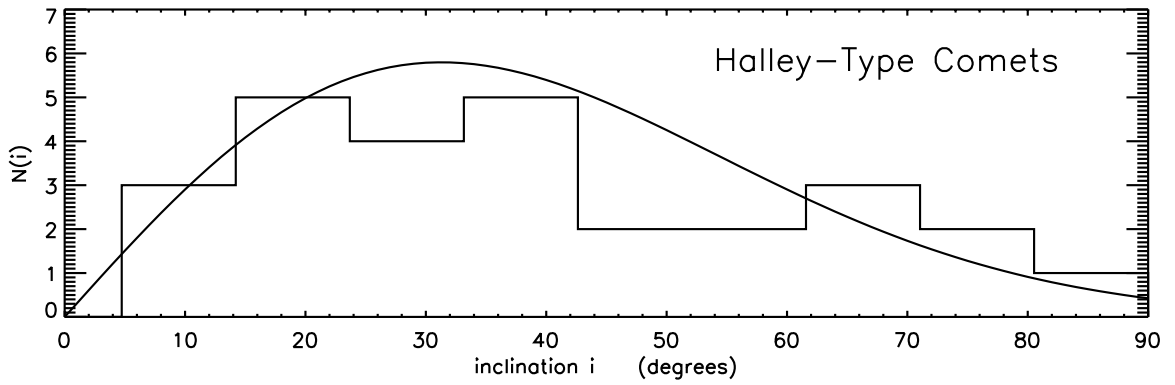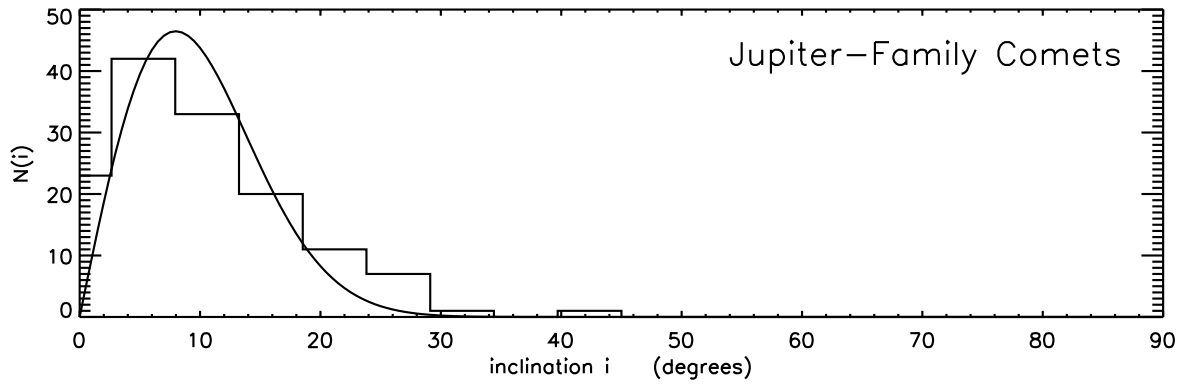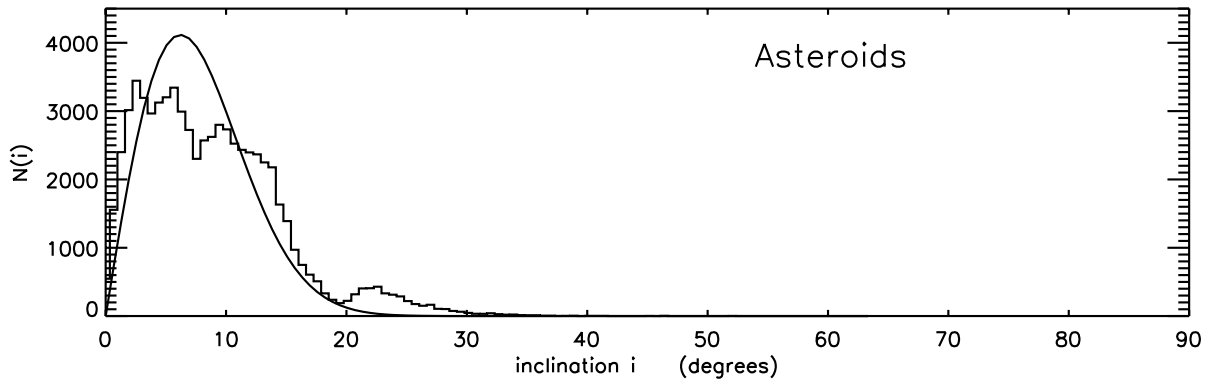
Fig. 10.— The upper figure shows the inclination distribution $N(i)$ for 70,383 asteroids having semimajor axes $a \leq 6$ AU brighter than absolute magnitude $H = 15$ (*i.e*, brighter than the completeness limit for asteroid surveys); this corresponds to asteroids having diameters between 5 and 850 km. These data come from Edward Bowell's *The Asteroid Orbital Elements Database* obtained from the URL ftp://ftp.lowell.edu/pub/elgb/astorb.html. Also shown are the inclination distributions for 138 Jupiter–Family comets (JFCs), 27 Halley–Type comets (HTCs), and 223 Oort Cloud comets (OCCs). Only those comets having perihelia $q < 2.5$ AU listed in the Marsden and Williams (1999) catalog are used here. The smooth curves are $g(i) \propto \sin(i)e^{-(i/\sigma)^2/2}$ with $\sigma = 6.2°$ for the asteroids, $\sigma = 8.0°$ for the JFCs, $\sigma = 33°$ for the HTCs, and $g(i) \propto \sin(i)$ for the OCCs. Since this study of the zodiacal light is insensitive to prograde versus retrograde orbits, we have replaced each retrograde orbit having an inclination $i > 90°$ with a prograde equivalent having an inclination $180° - i$ in order to improve the statistical significance of these figures.
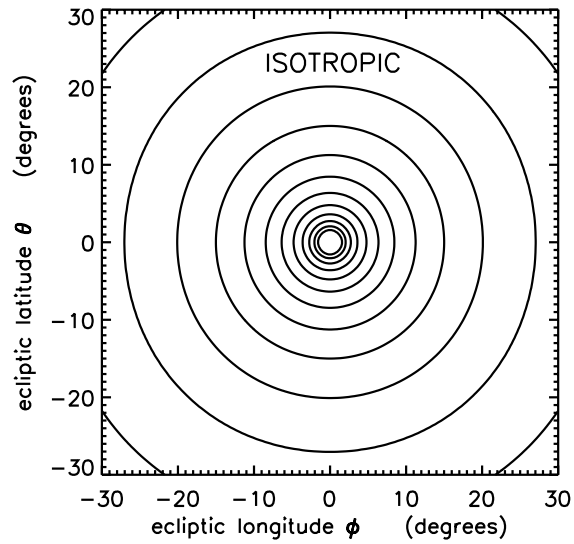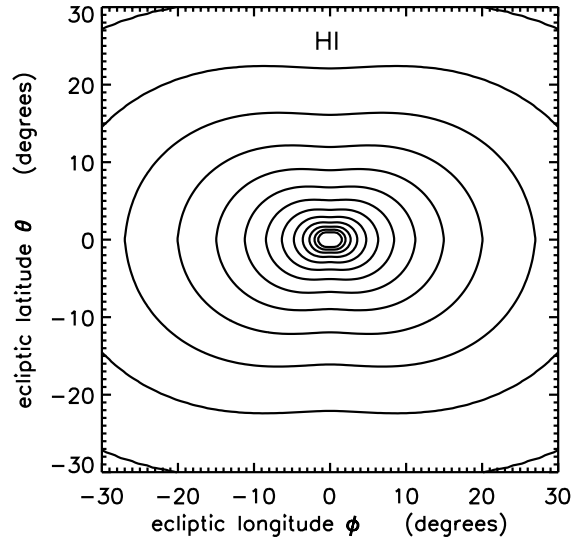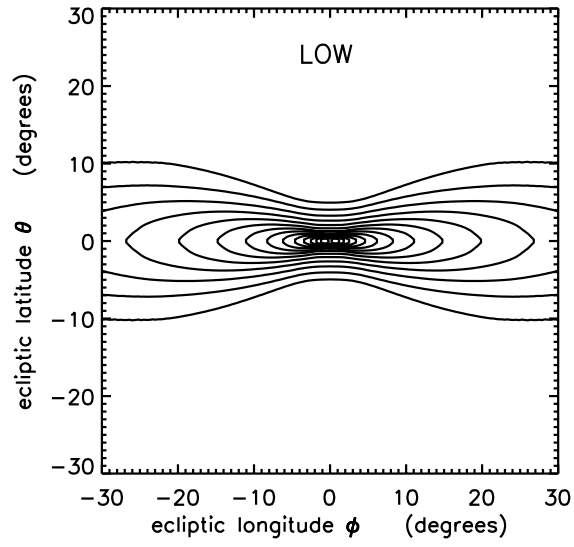
Fig. 11.— Isophotes for the low-inclination dust population (e.g., dust from asteroids and JFCs), the high–inclination population (dust from HTCs), and the isotropic population (dust from OCCs and interstellar sources). These contours are computed using Eq. 3 and the Hong phase law shown in Fig. 7 and with the dust cross sectional density varying as $\sigma(r) \propto r^{-\nu_j}$ with $\nu_j = 1.45$ for each population. The brightness of each isophote differs by a factor of 2. Isophotes for populations with $\nu_j = 1$ are shaped similarly but are shifted inwards while $\nu_j = 2$ isophotes are shifted outwards.
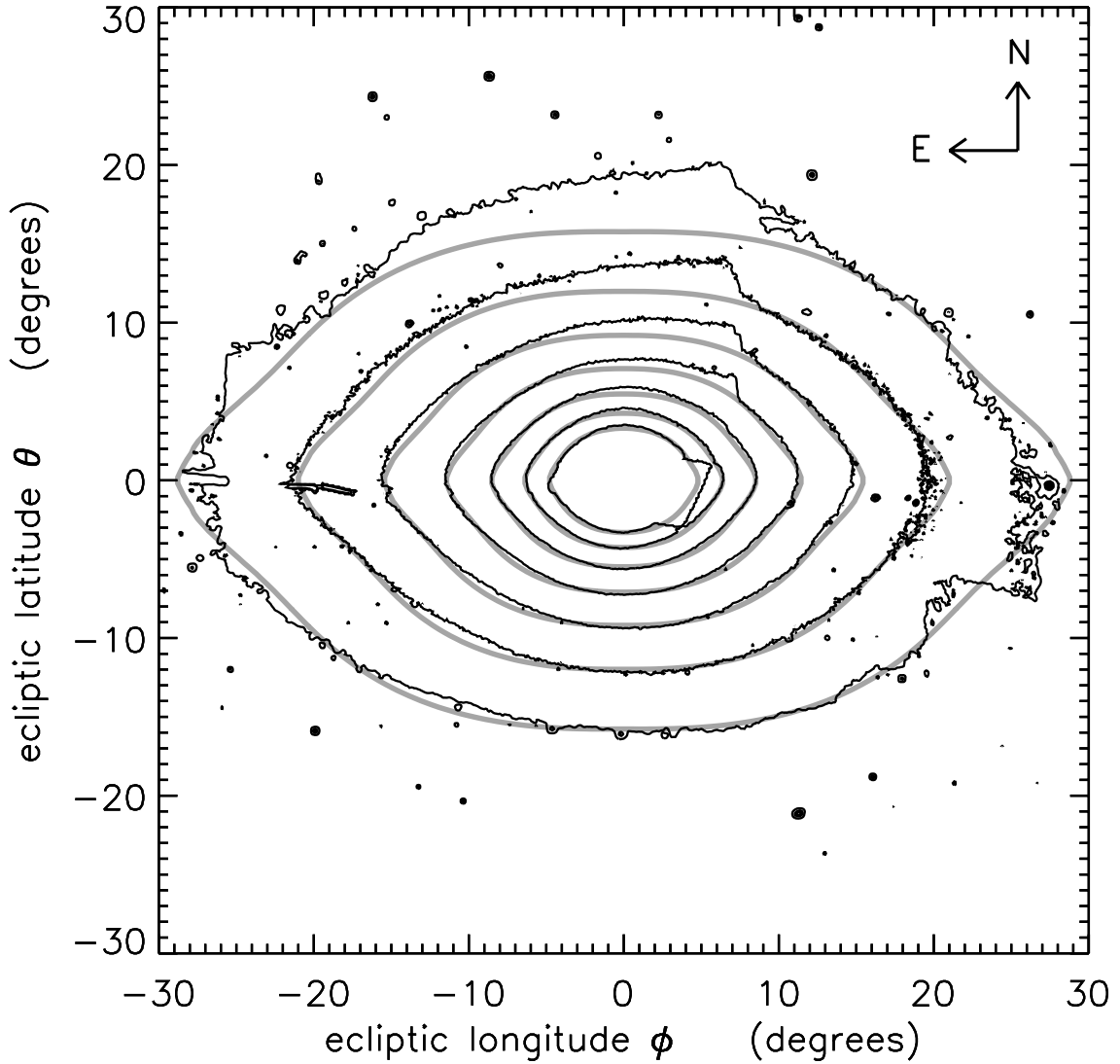
Fig. 12.— The narrow black curves are isophotes of the zodiacal light map of Fig. 5, and the thick grey curves are isophotes for the best–fitting model having the parameters given in Table II. The brightest isophote corresponds to a surface brightness of 7.45×10^{-11} $B_\odot$ and successive isophotes are dimmer by factors of 2. The outermost isophote is smoothed over a box 5 pixels or $0.38°$ wide. The rectilinear features seen in the outermost isophote are 'seams' in the mosaic image (see Fig. 5); they are due to small errors in the offsets δf that were removed from each image (see Section 3). The jag in the innermost contour as well as the linear features seen at $\phi = -20°$ and $-27°$ east of the Sun are all due to gaps in the data, and the bends in the isophotes north–northwest of the Sun are due to scattered light in the camera.
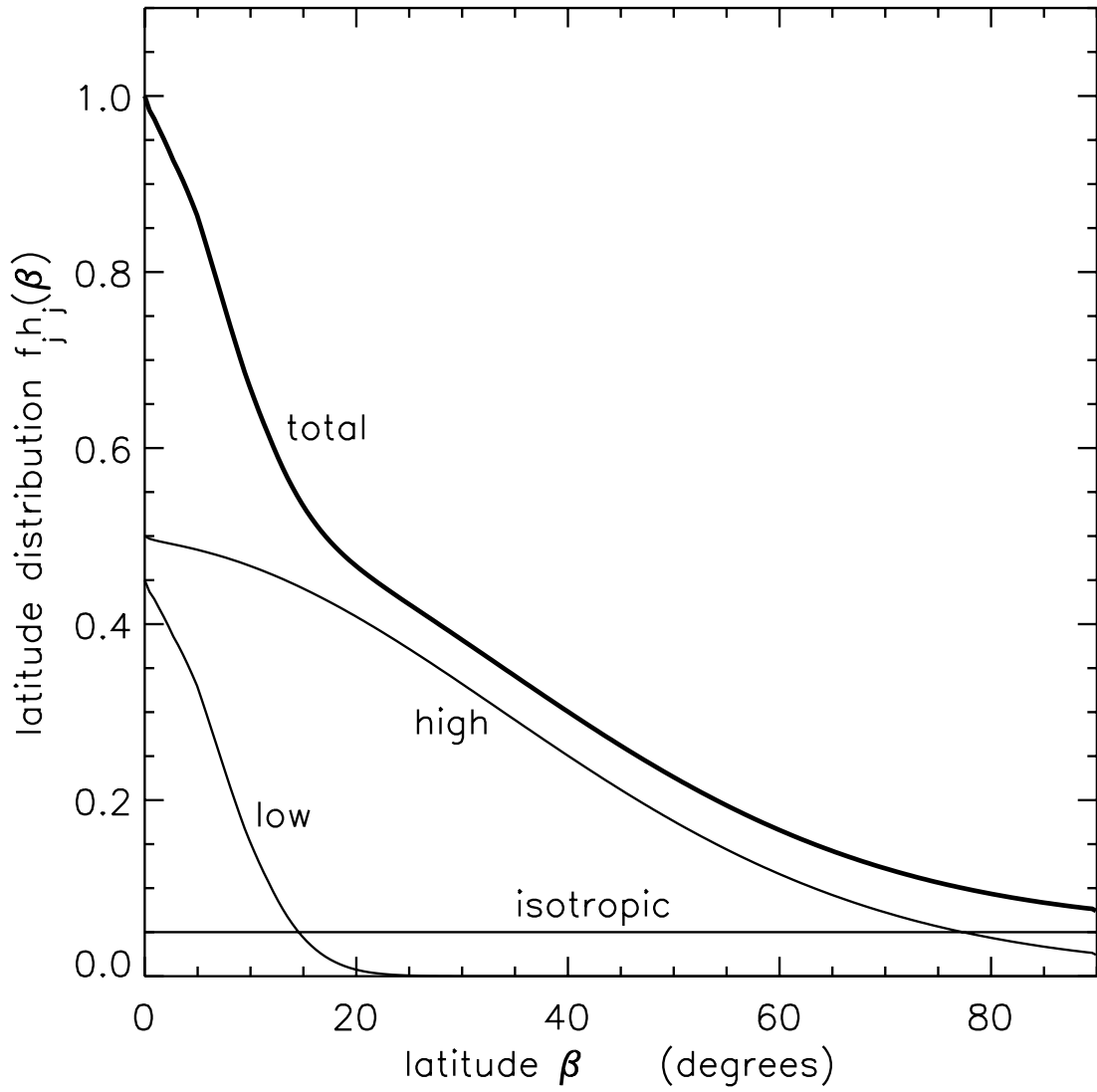
Fig. 13.— The total dust latitude distribution $h(\beta)$ plotted versus heliocentric ecliptic latitude β. Also shown are the weighted contributions by the low, high, and isotropic populations, $f_j h_j(\beta)$.
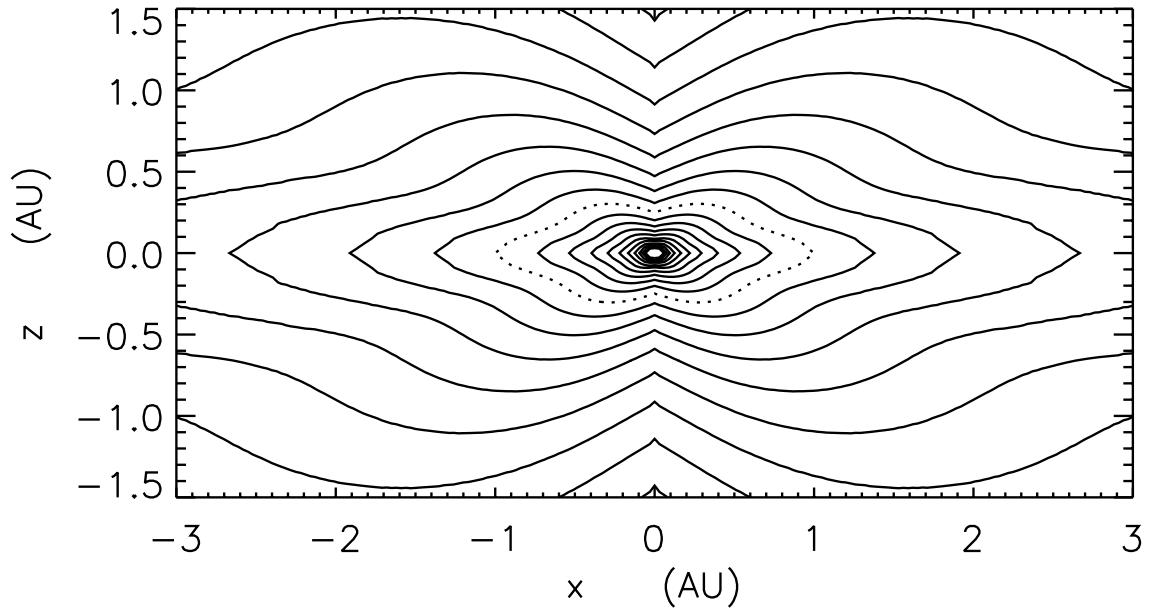
Fig. 14.— Contours of the inferred density of dust cross–section $\sigma(x, z)$ in cylindrical coordinates where x is the ecliptic distance from the Sun and z the height above the ecliptic plane. Adjacent contours indicate a factor of 1.5 change in the dust density and the dotted curve is where the dust density $\sigma(x, z) = \sigma_1 = 4.6 \times 10^{-21}$ cm^2/cm^3.
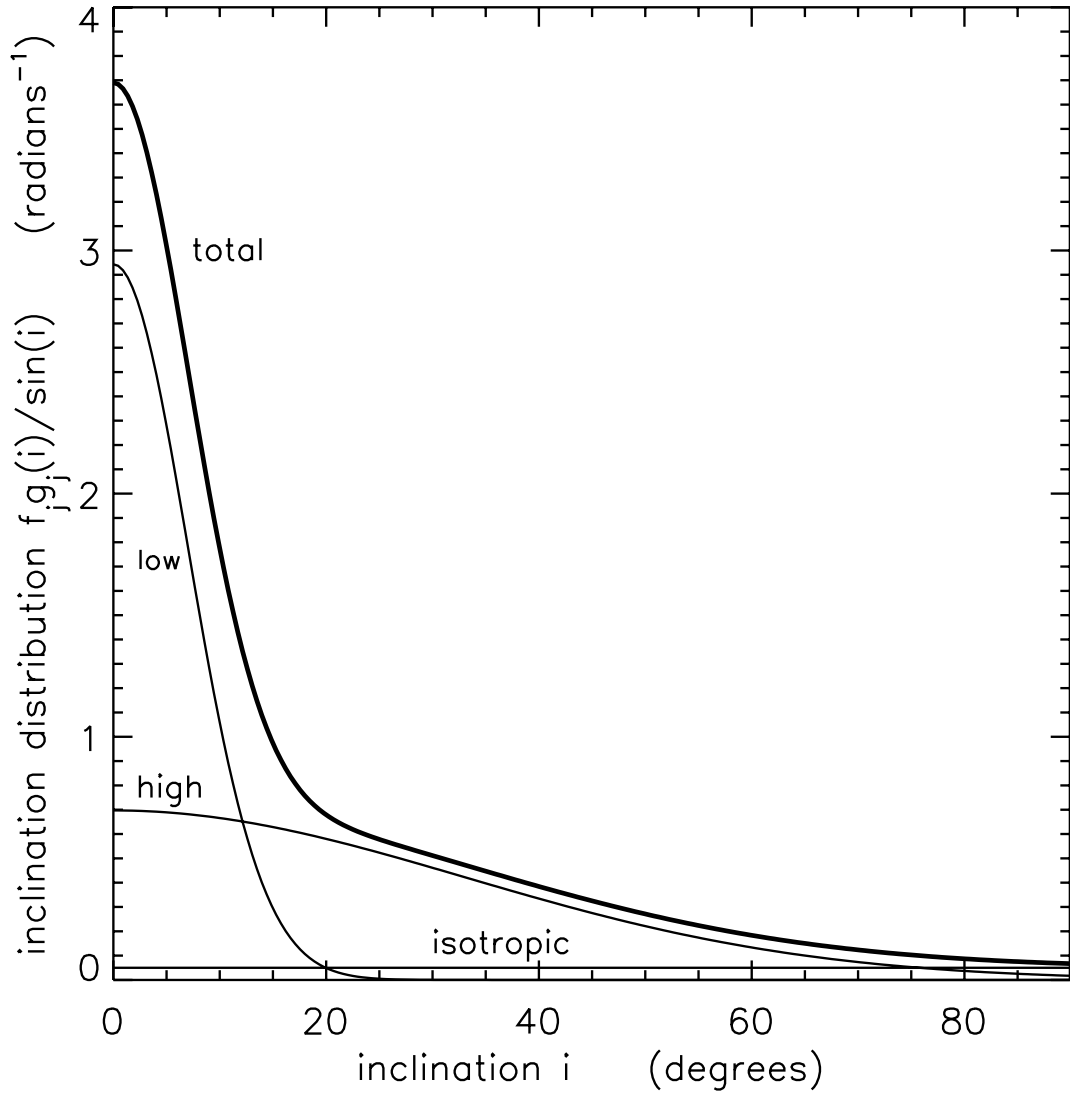
Fig. 15.— The total inclination distribution $g(i)/\sin i$ plotted versus inclination i as well as the weighted contributions from the low, high, and isotropic populations.
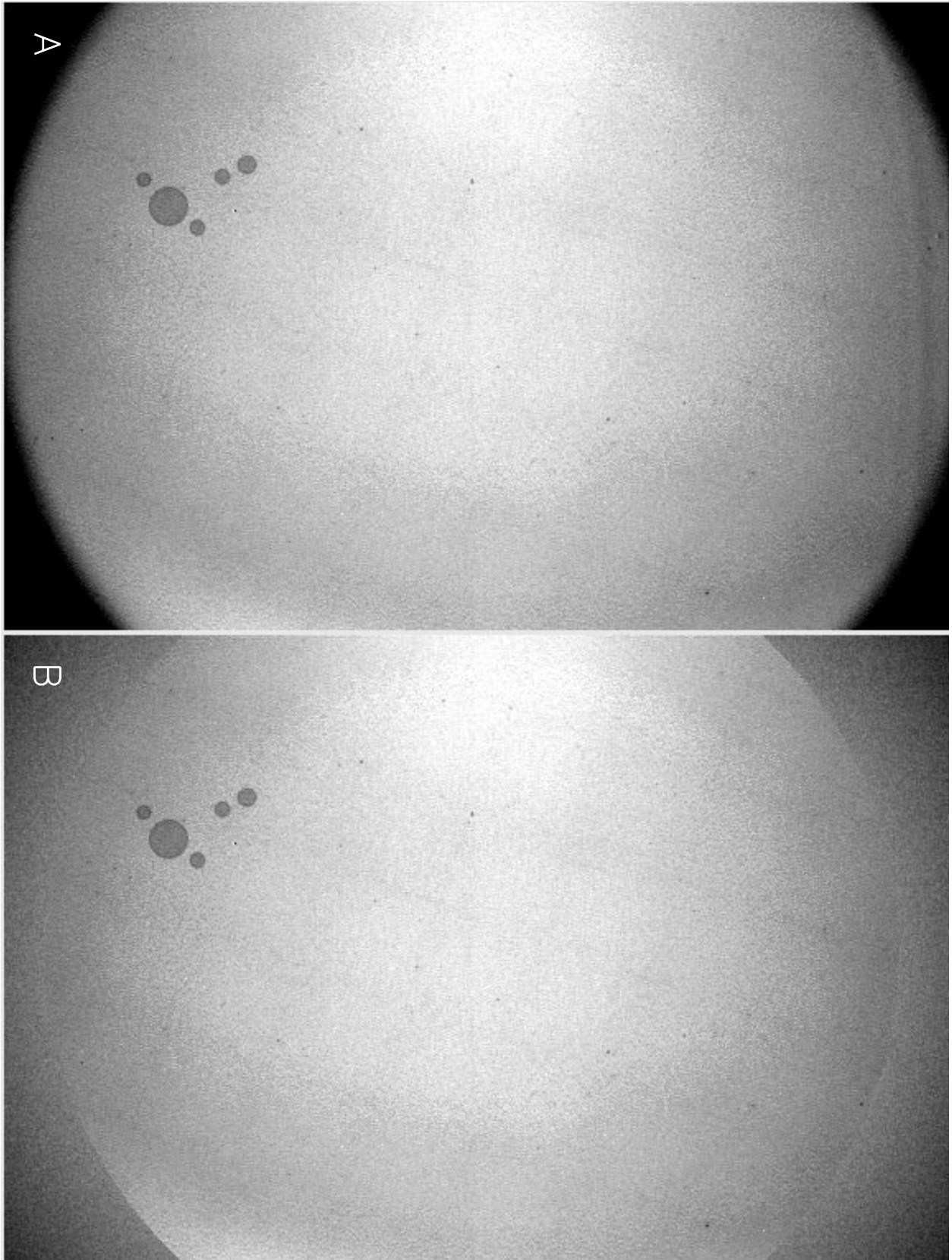
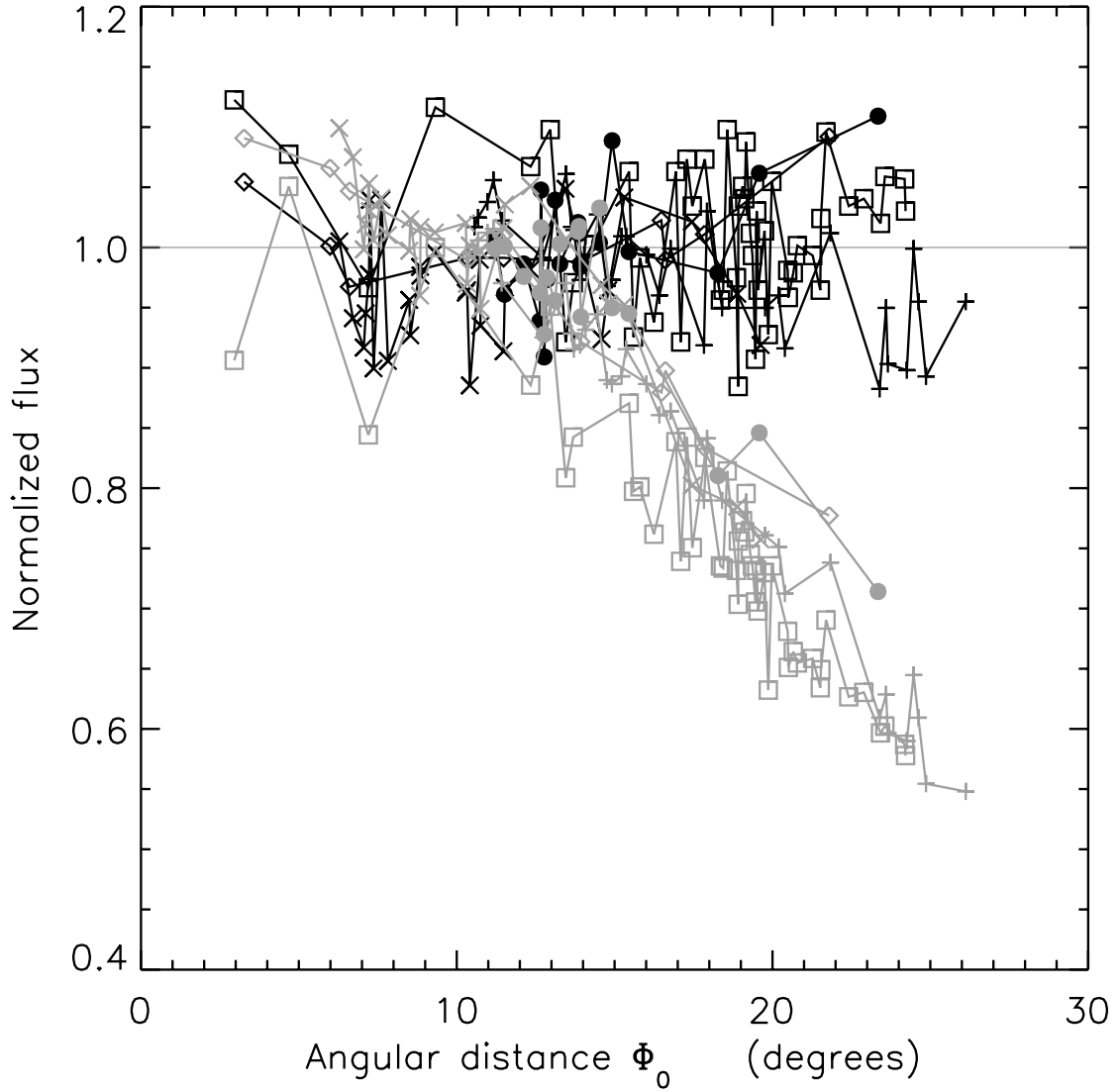Fig. 16.— **A**. The vignetted flatfield. **B**. The reconstructed flatfield.

Fig. 17.— The intensities of five stars (indicated by different plotting symbols) seen in different images acquired during orbit 66 are plotted versus each star's angular distance from the optical axis Φ_0. All intensities are normalized to unity near $\Phi_0 = 0$. The grey curves are extracted from images that are not flatfielded, and the dark curves are from images obtained with the reconstructed point–source flatfield.